

Structural phase transitions and photoluminescence mechanism in a layer of 3D hybrid perovskite nanocrystals

Yuri D. Glinka,^{1,2,a)} Rui Cai,¹ Xian Gao,¹ Dan Wu,¹ Rui Chen,^{1,b)} and Xiao Wei Sun^{1,3,c)}

¹Guangdong University Key Lab for Advanced Quantum Dot Displays and Lighting, Shenzhen Key Laboratory for Advanced Quantum Dot Displays and Lighting, Department of Electrical & Electronic Engineering, Southern University of Science and Technology, Shenzhen 518055, China

²Institute of Physics, National Academy of Sciences of Ukraine, Kiev, 03028, Ukraine.

³Shenzhen Planck Innovation Technologies Pte Ltd, Ganli 6th Road, Longgang, Shenzhen 518112, China

^{a)}yuri@sustc.edu.cn, yuridglinka@yahoo.com

^{b)}chenr@sustc.edu.cn

^{c)}sunxw@sustc.edu.cn

Although the structural phase transitions in single-crystal hybrid methyl-ammonium (MA) lead halide perovskites (MAPbX_3 , $X = \text{Cl, Br, I}$) are common phenomena, they have never been observed in the corresponding nanocrystals. Here we demonstrate that two-photon-excited photoluminescence (PL) spectroscopy is capable of monitoring the structural phase transitions in MAPbX_3 nanocrystals compared to conventional one-photon-excited PL spectroscopy because nonlinear susceptibilities govern the light absorption rates. Using this technique, we provide experimental evidence that the orthorhombic-to-tetragonal structural phase transition in a single layer of 20-nm-sized 3D MAPbBr_3 nanocrystals is spread out within the $\sim 70 - 140$ K range. This structural phase instability range arises because, unlike in single-crystal MAPbX_3 , free rotations of MA ions in the corresponding nanocrystals are no longer restricted by a long-range MA dipole order. The resulting configurational entropy loss and the corresponding liquid-like motion of MA cations can be even enhanced by the interfacial electric field arising due to charge separation at the $\text{MAPbBr}_3/\text{ZnO}$ heterointerface, extending the orthorhombic-to-tetragonal structural phase instability range from 70 to 230 K. We conclude that the weak sensitivity of conventional one-photon-excited PL spectroscopy to the structural phase transitions in 3D MAPbX_3 nanocrystals results from the structural phase instability providing negligible distortions of PbX_6 octahedra responsible for the band-edge electronic transitions. In contrast, the intensity of two-photon-excited PL and electric-field-induced one-photon-excited PL still remains sensitive enough to weak structural distortions due to the higher rank tensor nature of nonlinear susceptibilities involved. We also show that room-temperature PL originates from the radiative recombination of the optical-phonon vibrationally excited polaronic quasiparticles with energies might exceed the ground-state Fröhlich polaron and Rashba energies due to optical-phonon bottleneck. Because of small masses and large radii of these vibrationally excited polaronic quasiparticles, their high mobility and long-range diffusion become possible.

I. INTRODUCTION

Hybrid methyl-ammonium (MA) lead halide perovskites (MAPbX₃, X = Cl, Br, I) represent a class of materials offering an illustrative platform for studying the relaxation dynamics of photoexcited carriers and their transport phenomena in novel highly efficient solar cells for solar energy harvesting technology.¹⁻¹¹ One of the most important specific features of these hybrid materials is that their crystalline structure can be viewed as two alternating sublattices. Specifically, the inorganic sublattice is composed by corner-sharing PbX₆ octahedra which are responsible for forming the valence band (VB) maximum and conduction band (CB) minimum of these materials.^{7,8} Consequently, the initial relaxation of photoexcited carriers, their recombination and transport phenomena all occur in the inorganic sublattice. Alternatively, the organic MA sublattice acts as a medium modifying the electrostatic potential of the inorganic sublattice, thus contributing less significantly to the charge screening and localization effects, nevertheless, providing an ultralow thermal conductivity being caused by long-range MA dipole order.¹² The structural peculiarities of these materials allow for the three structural phase transitions occurring in the temperature range of $T \sim 140 - 240$ K, which usually appear in single-crystal MAPbX₃ and its polycrystalline thin film,¹³⁻²⁵ whereas they have never been observed in MAPbX₃ nanocrystals.²¹

Because arrays of colloidal nanocrystals are known to be promising alternatives to the single-crystal semiconductor based electronics, optoelectronics, and solar energy harvesting applications²⁶ and because the properties of single-crystal MAPbX₃ differ significantly for different structural phases,¹³⁻²⁵ we comprehensively explored the structural phase transitions in a fully encapsulated single layer of 20-nm-sized 3D MAPbBr₃ nanocrystals using one-photon-excited and two-photon-excited PL spectroscopy. The effect of the technologically important MAPbBr₃/ZnO heterointerface on this phenomenon has also been studied here. We show that two-photon-excited PL spectroscopy and electric-field-induced one-photon-excited PL spectroscopy are capable of more precisely monitoring the structural phase transitions in 3D MAPbBr₃ nanocrystals compared to conventional one-photon-excited PL spectroscopy since nonlinear susceptibilities govern the light absorption rates. Consequently, one can recognize that the orthorhombic-to-tetragonal structural phase transition in 3D MAPbBr₃ nanocrystals, unlike in single-crystal MAPbX₃, is spread out over the broad temperature range of $T \sim 70 - 140$ K. This extension of the structural phase transition defines the structural phase instability range, within which the local field fluctuations arising due to free rotations of MA ions are no longer restricted by long-range polar order.^{27,28} The resulting configurational entropy loss and the corresponding liquid-like motion of MA cations¹ can be even enhanced by the interfacial electric field when charge separation at the MAPbBr₃/ZnO heterointerface occurs, extending the orthorhombic-to-tetragonal structural phase instability range from $T \sim 70$ to 230 K. The latter effect is found to be dependent on the ZnO layer thickness and the photoexcited carrier density. Finally, we conclude that a stepwise shift of the PL band with temperature observed for single-crystal MAPbX₃ and assigned to structural phase transitions does not appear anymore in 3D MAPbX₃ nanocrystals because of negligible distortions of PbX₆ octahedra under the structural phase instability regime. On the contrary, the nearly monotonic blue shift of PL band with increasing temperature in a fully encapsulated single layer of 20-nm-sized

3D MAPbBr₃ nanocrystals seems to result rather from the heating effect under TO/LO phonon bottleneck²⁻⁴ than that being induced by the progressive PbX₆ octahedra distortions. Consequently, room-temperature PL is expected to originate from the radiative recombination of the optical-phonon vibrationally excited polaronic quasiparticles with energies might exceed the ground-state Fröhlich polaron and Rashba energies due to optical-phonon bottleneck. Because of small masses and large radii of these vibrationally excited polaronic quasiparticles, their high mobility and long-range diffusion become possible.

II. EXPERIMENTAL

A. Sample fabrication

The size-controlled CH₃NH₃PbBr₃ nanocrystals were synthesized by a ligand-assisted reprecipitation (LARP) technique.²⁹ The CH₃NH₃Br precursor was synthesized by adding hydrobromic acid (HBr, 48 wt.% in H₂O, 99.99%; Sigma-Aldrich) drop wise to a stirred solution of methylamine (CH₃N, 30~33 wt.% in ethanol) at 0 °C followed by stirring for 1 h. Upon drying at 100 °C in air, white CH₃NH₃Br powder in quantitative yield was formed. After being washed with diethyl ether (Shanghai Lingfeng Chemical Reagents) and recrystallized with ethanol, CH₃NH₃Br powder was dried for 24 h in a vacuum furnace and along with other precursors was added into the N,N-dimethylformamide (DMF, C₃H₇NO, anhydrous, 99.8%). Specifically, CH₃NH₃Br and lead (II) bromide (PbBr₂, powder, 98%) were dissolved in 100 μL DMF forming a mixture with a concentration of 0.1 mM and then 200 μL oleic acid (C₁₈H₃₄O₂; Aladdin) and 20 μL oleylamine (C₁₈H₃₇N, 80~90%; Aladdin) were added into this mixture. The oleic acid/oleylamine ligand ratio was selected for tailoring the size of the nanocrystals. The 100 μL mixture of various precursors was injected afterwards into 3 mL chloroform (Shanghai Lingfeng Chemical Reagents) as an antisolvent. A yellow-greenish colloidal solution was acquired afterwards. For further purification, 1.5 mL toluene/acetonitrile (CH₃CN, anhydrous, 99.8%) mixture with a volume ratio 1:1 was added into the solution and the sediment was dispersed in hexane after centrifuging at 9000 rpm for 2 min.

To prepare the fully encapsulated layer of 3D CH₃NH₃PbBr₃ nanocrystals, the sapphire plates (10×10×0.3 mm; Jiangsu Hanchen New Materials) were cleaned by successively soaking them in an ultrasonic bath with deionized water, acetone, and isopropanol for 10 min each and dried with nitrogen. The sapphire substrates were transferred afterwards into the atomic layer deposition (ALD) system (PICOSUN™ R-200) to grow a ZnO film. Diethyl zinc (DEZn, Zn(C₂H₅)₂) and H₂O were used as precursors. High purity nitrogen with dew point below -40 °C was used as a purging and carrier gas. The reactor chamber pressure was set as 1000 Pa during the growth. When the growth temperature of 200 °C was reached, DEZn was introduced to the reactor chamber with a flow rate of 150 sccm followed by purging with nitrogen to remove the residues and byproducts. The precursor of H₂O with a flow rate of 200 sccm was introduced afterwards into the reactor chamber to start with the ZnO layer growth. The number of ALD growth cycles was selected to grow a ZnO layer with thicknesses of 30 and 100 nm, which were also verified by other methods.

Closely packed and uniformly distributed CH₃NH₃PbBr₃ nanocrystals were spin-coated afterwards by optimizing the spin speed to 1500 rpm to either the clean sapphire (Sa) plate or to those initially ALD-coated with a ZnO layer of 30 nm and 100

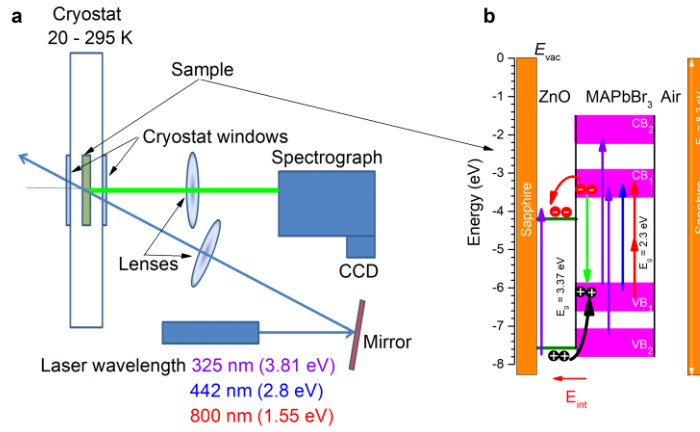


FIG. 1 (a) A sketch of the experimental setup. (b) A band alignment of a fully encapsulated layer of MAPbBr₃ nanocrystals spin-coated to the ALD-grown ZnO layer. The charge separation process at the MAPbBr₃/ZnO heterointerface and the resulting interfacial electric field (E_{int}) are shown. Laser wavelengths indicated in (a) and the corresponding electronic transitions indicated in (b) are shown by the same colors.

nm thickness. The resulting structure was covered by another sapphire plate, leaving the air gap above the nanocrystal array of $\sim 1 \mu\text{m}$ and gluing sapphire plates on sides by UV adhesive. The obtained samples will be referred further below as MAPbBr₃/Sa, MAPbBr₃/ZnO(30nm) and MAPbBr₃/ZnO(100nm), respectively.

B. Scanning electron microscopy (SEM) imaging.

The cross-sectional SEMs images of the sandwiched samples were acquired using a ZEISS Gemini 300 field emission scanning electron microscope in a secondary electron mode after cleaving the samples with a diamond scribe.

C. Transmission electron microscopy (TEM) imaging

The crystallinity of the synthesized CH₃NH₃PbBr₃ nanocrystals was confirmed by TEM imaging (Tecnai F30 field-emission TEM) operated at 300 kV and at room temperature.

D. X-ray diffraction (XRD) characterization

The XRD patterns of the synthesized CH₃NH₃PbBr₃ nanocrystals were measured using a Rigaku SmartLab X-ray diffractometer, equipped with a Cu KR radiation source (wavelength at 1.542 Å). The samples were scanned from $10^\circ < 2\theta < 60^\circ$ at an increment of $10^\circ/\text{min}$.

E. Conventional ultraviolet–visible absorption and PL characterization

The conventional absorption spectra were measured at room temperature using the Beijing Spectrum Analysis 1901 Series spectrometer. To study PL spectra, the Ocean Optics QE 65 Pro spectrometer equipped with a 365 nm excitation source was used with a spectral resolution of $\sim 1.0 \text{ nm}$.

F. Temperature-dependent PL measurements

To study temperature-dependent PL spectra, the commercially available temperature controller (Lakeshore 336) with a temperature range of 20 - 295 K was used. The PL spectra were measured using the Andor Shamrock SR750 spectrograph

equipped with a CCD detector. Figure 1a shows a sketch of the experimental setup for measuring the temperature dependent PL from a layer of 3D MAPbBr₃ NCs. Three laser wavelengths were used to excite PL: 325, 442, and 800 nm, which were emitted from the CW He-Cd laser (325 and 442 nm) and the femtosecond laser (Astrella-Tunable-V-F-1K) with the pulse width of 100 fs and a repetition rate of 1.0 KHz (800 nm). The laser beam incidence angle was 30° . The sample holder was designed to allow the excitation laser light to pass through the sample and the cryostat windows, being blocked afterwards outside the cryostat. Such an arrangement eliminates any additional spectroscopic features associated with the scattering and reabsorption of laser light from the sample holder to appear in PL spectra. The laser spot diameter was $\sim 250 \mu\text{m}$ for all the three excitation wavelengths. The excitation power was changed by a variable neutral density filter (Thorlabs). The averaged laser power varied from 0.03 to 20 mW for the CW He-Cd laser and from 2.0 to 30 mW for the pulsed laser. For the experimental conditions applied, 1.0 mW average laser power corresponds to the laser light intensity (power density) of 2.04 W/cm^2 for the CW laser and 20.5 GW/cm^2 for the pulsed laser. Taking into account the measured one-photon absorption coefficient ($\sim 4.0 \times 10^4 \text{ cm}^{-1}$ and $\sim 1.9 \times 10^4 \text{ cm}^{-1}$ for 325 and 442 nm laser light, respectively) and the two-photon absorption coefficient of $\sim 8.6 \text{ cm}/10^9 \text{ W}$,³⁰ the reflectance coefficient of 0.37 and estimating afterwards the power density absorbed within the CH₃NH₃PbBr₃ nanocrystal array,³¹ the corresponding photoexcited carrier densities were calculated to be $\sim 7.5 \times 10^{17} \text{ cm}^{-3}$ ($\sim 7.5 \times 10^{-4} \text{ nm}^{-3}$), $\sim 4.9 \times 10^{17} \text{ cm}^{-3}$ ($\sim 4.9 \times 10^{-4} \text{ nm}^{-3}$), and $\sim 1.7 \times 10^{18} \text{ cm}^{-3}$ ($\sim 1.7 \times 10^{-3} \text{ nm}^{-3}$) for 325, 442, and 800 nm laser light, respectively. Assuming the nanocrystal cubic shape of the same edge length of $\sim 20 \text{ nm}$ (the corresponding volume is $\sim 8 \times 10^3 \text{ nm}^3$), the average electron-hole pair occupancy per nanocrystal can be estimated as ~ 6.0 , ~ 3.9 , and ~ 13.6 , respectively. However, multiple excitons photoexcited in a nanocrystal is believed to be non-interactive since their small effective exciton Bohr radius in MAPbX₃ perovskite materials (2.0 – 4.0 nm),

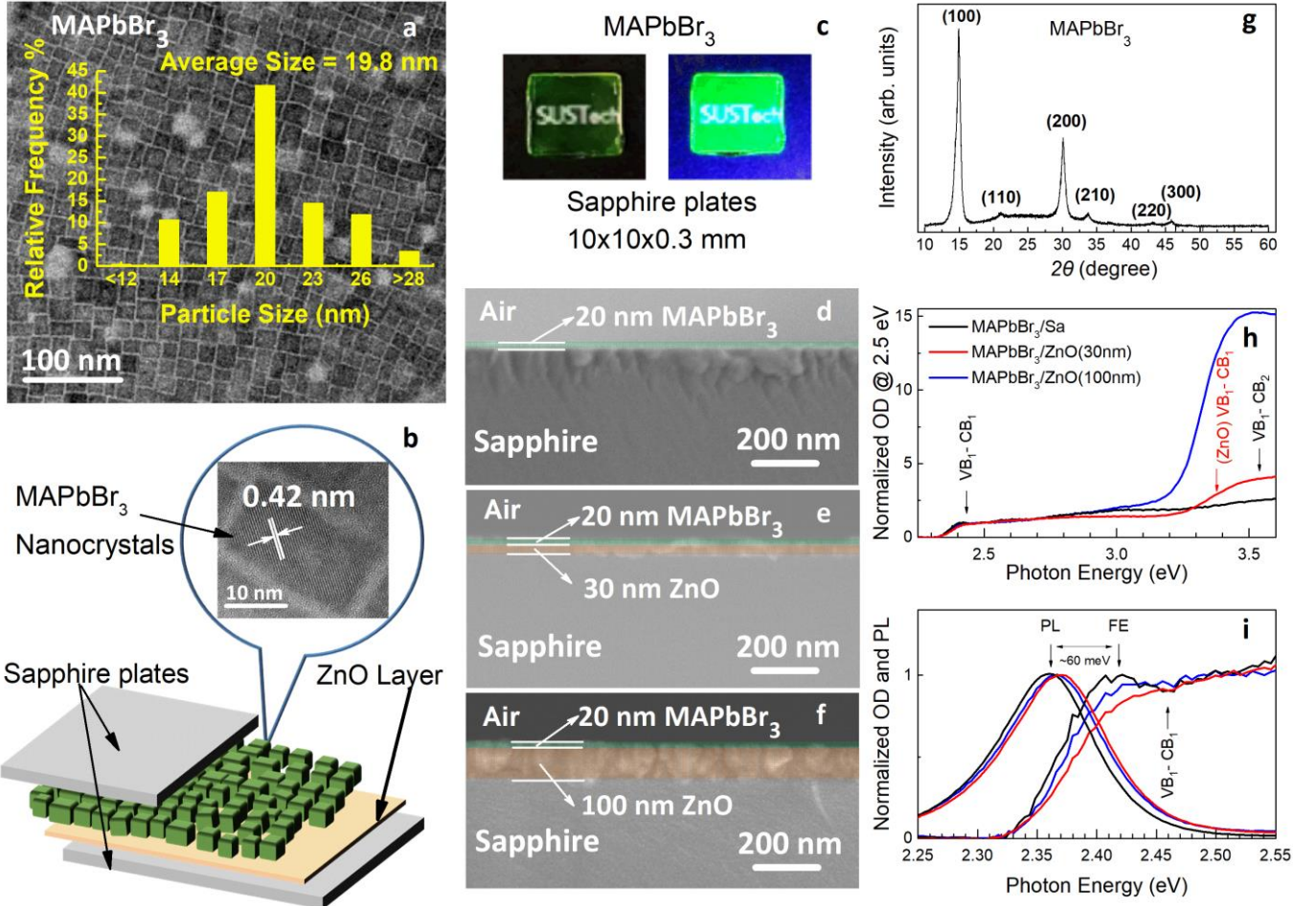


FIG. 2 (a) The TEM image of 3D MAPbBr₃ nanocrystals. The corresponding histogram demonstrates the nanocrystal size distribution. (b) A schematic presentation of the encapsulated layer of 3D MAPbBr₃ nanocrystal and the high-resolution TEM image of an individual MAPbBr₃ nanocrystal. (c) A real image of a layer of 3D MAPbBr₃ nanocrystals illuminated by daylight (left) and UV light (right). The white color “SUSTech” label placed behind the sample demonstrates its transparency. (d)-(f) The cross-sectional SEM views of the MAPbBr₃/Sa, MAPbBr₃/ZnO(30nm), and MAPbBr₃/ZnO(100nm) samples, respectively. (g) The XRD pattern of MAPbBr₃ nanocrystals with the corresponding Miller indexes labelled. (h) and (i) The room temperature conventional absorption (optical density - OD) and PL spectra measured for three samples identified in (d)-(f). The transitions between VB and CB of MAPbBr₃ and ZnO are indicated. The Stokes shift was estimated as a photon energy difference between the FE peak in absorption spectra and the PL peak.

compared, for example, to GaAs (~12 nm),³² as will be discussed further below in details.

III. RESULTS AND DISCUSSION

A. Sample characterization

Figure 2(a) shows the TEM image of the as-grown colloidal cubic-shaped MAPbBr₃ nanocrystals together with the corresponding histogram presenting the nanocrystal size distribution which is maximized at $\sim 19.8 \pm 1.7$ nm. The high-resolution TEM image [Fig. 2(b)] and XRD pattern [Fig. 2(g)] confirms the high crystallinity and 3D structure of the individual MAPbBr₃ nanocrystal with the typical characteristic lattice fringes spaced by ~ 0.42 nm.^{29,33-39} Figure 2(b) also shows schematically the method of fully encapsulating MAPbBr₃ nanocrystals between the two sapphire plates. The fully encapsulated MAPbBr₃ nanocrystals demonstrate stable optical properties (at least for 4 months within which various optical measurements were performed), such as high transparency and uniform PL [Fig. 2(c)]. The thickness of MAPbBr₃ layer viewed by SEM is comparable to the size of nanocrystals [Fig. 2(d)-(f)],

thus suggesting that no more than one layer of the closely packed MAPbBr₃ nanocrystals was deposited. Because 3D MAPbX₃ nanocrystals are known to be the basic building blocks for growing the corresponding nanoplates and nanowires, that is, 2D and 1D structures,^{35,38} our samples can also be identified as quasi-2D arrays of 3D CH₃NH₃PbBr₃ nanocrystals to distinguish them from the 2D layered counterpart of hybrid perovskites [(C₄H₉NH₃)₂PbBr₄].³⁸

Figure 2(h) and (i) shows the room-temperature conventional absorption and PL spectra of the MAPbBr₃/Sa, MAPbBr₃/ZnO(30nm), and MAPbBr₃/ZnO(100nm) samples identified in Fig. 2(d)-(f). The absorption spectrum of the MAPbBr₃/Sa sample reveals two contributions associated with electronic transitions from VB to two CBs.^{40,41} The ZnO layer additionally contributes to absorption spectra in the UV range for the MAPbBr₃/ZnO samples [Fig. 2(h)].⁴² The Stokes shift was estimated as $\hbar\Delta\omega_{\text{Stokes}} = \lambda_e + \lambda_h = \sim 60$ meV, where \hbar is the reduced Planck constant, $\Delta\omega_{\text{Stokes}}$ is the frequency difference between the 1s free exciton (FE) peak in absorption spectra and the PL peak, and λ_e and λ_h are the corresponding reorganization

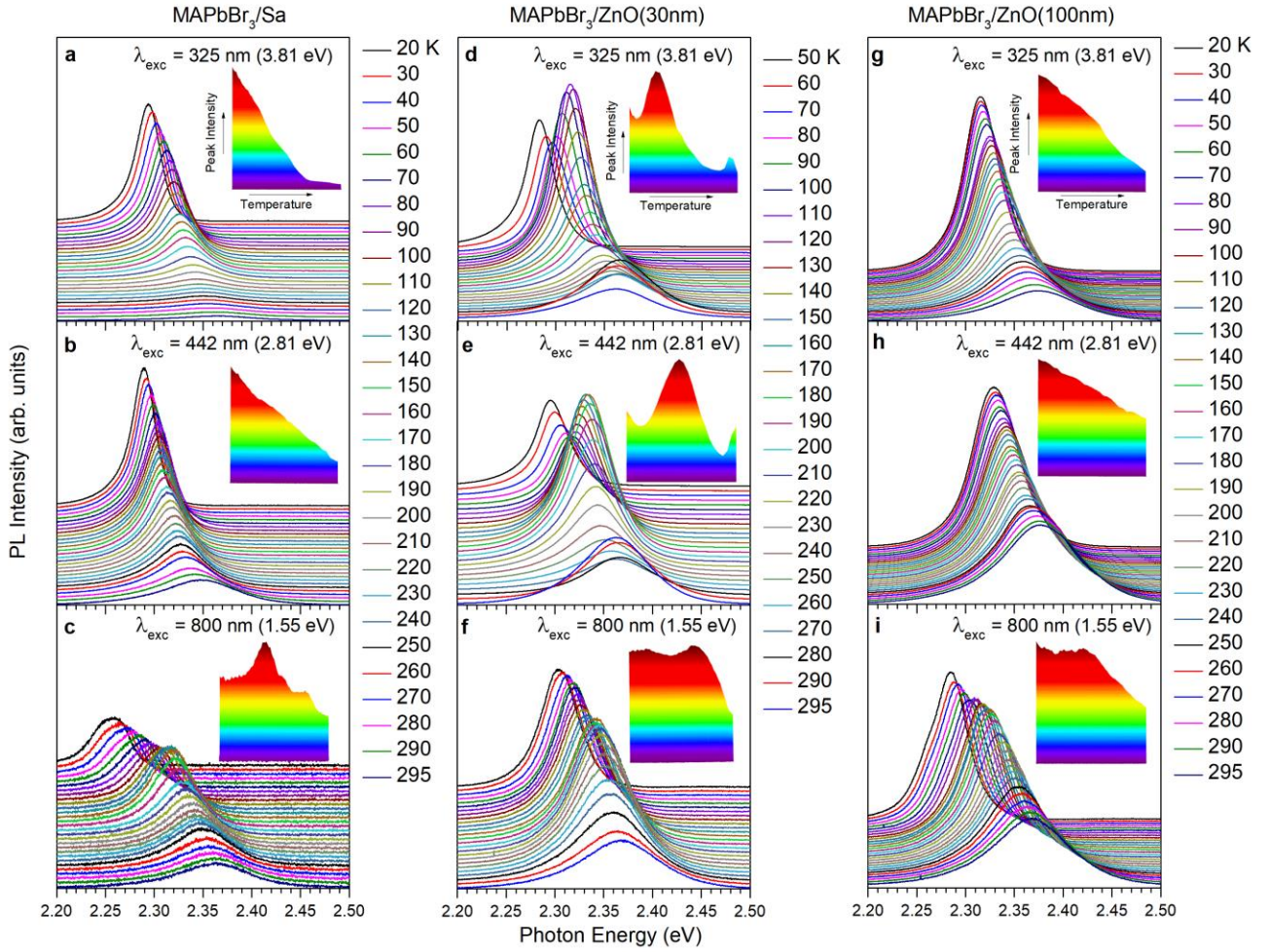


FIG. 3 PL spectra measured for the MAPbBr₃/Sa (a) – (c), MAPbBr₃/ZnO(30nm) (d) – (f), and MAPbBr₃/ZnO(100nm) (g) – (i) samples at different temperatures, as indicated by the corresponding colors, and with different excitation photon energies, as indicated for each of the panels. The individual baselines for each of the spectra are arbitrary shifted for better observation. The color map graphs present the corresponding variations of the PL-peak intensity with increasing temperature.

energies⁴³ for electrons and holes, respectively. The latter quantities characterize hence the band gap renormalization appearing as the energetic difference between the unrelaxed (non-equilibrium) and relaxed (equilibrium) carriers, which can be estimated in the frame of the Fröhlich large polaron model^{9,44} as $\lambda_e \sim 32.6$ meV and $\lambda_h \sim 39.2$ meV for the longitudinal-optical (LO)-phonons contribution. The intensity of the $1s$ FE absorption peak decreases in MAPbBr₃/ZnO due to the interfacial-electric-field-induced FE dissociation, the process which balances the relative densities of free carriers and FEs.¹⁹ The more prominent suppression of the $1s$ FE absorption peak in the MAPbBr₃/ZnO(30nm) sample compared to the MAPbBr₃/ZnO(100nm) sample suggests that the interfacial electric field in the former is stronger than that in the latter. The exciton dissociation process is also accompanied by a blue-shift of PL-peak (~ 10 meV), which is greater in the MAPbBr₃/ZnO(30nm) sample as well [Fig. 2(i)]. These facts together with good coincidence between reorganization energies and the Stokes shift all confirm the FE nature of the band-edge light emission at room temperature. The latter statement is also well consistent with the large polaronic exciton binding energy in MAPbBr₃ (~ 35 meV),^{17,23} thus exceeding substantially the room temperature $k_B T = 25.7$ meV, where k_B is the Boltzmann

constant and T is the temperature. We also note that because the size of MAPbBr₃ nanocrystals (~ 20 nm) substantially exceeds the exciton Bohr radius (~ 2.0 nm),⁴⁵ any quantum-confinement-induced effects are expected to be negligible.

The typical phonons contributing to the temperature-dependent dynamics include the PbBr₆ octahedra twist mode (TO-type) with frequency ~ 40 cm⁻¹ (~ 5 meV) and the distortion mode (LO/TO-type) with frequency ~ 58 cm⁻¹ (~ 7.2 meV).^{46,47} The interaction between MA cations and PbBr₆ anions results in a broad MA torsional (MAT) mode peaked at ~ 300 cm⁻¹ (~ 37.2 meV), which governs the orientation dipole order of MA cations in the whole crystal.⁴⁶ MA internal (MAI) modes have much higher frequencies of $\sim 900 - 3200$ cm⁻¹ ($112 - 397$ meV).^{46,47} However, owing to a global lattice compression in nanocrystals,³⁶ the frequency of the LO-phonon mode observed for MAPbBr₃ nanocrystals increases to ~ 150 cm⁻¹ (~ 18.6 meV).^{48,49} Because the lattice compression varies with the nanocrystal size, TO/LO-phonon energy is expected to be spread over a few meV.⁴⁹ Consequently, we will refer further below to the following low-energy lattice vibrations: (i) the TO-phonon mode with averaged energy $\langle \hbar\omega_{TO} \rangle \sim 5.0$ meV, (ii) the LO-phonon mode with averaged energy $\langle \hbar\omega_{LO} \rangle \sim 18.6$ meV, (iii) the MAT-phonon modes with averaged energy $\langle \hbar\omega_{MAT} \rangle$ ranging

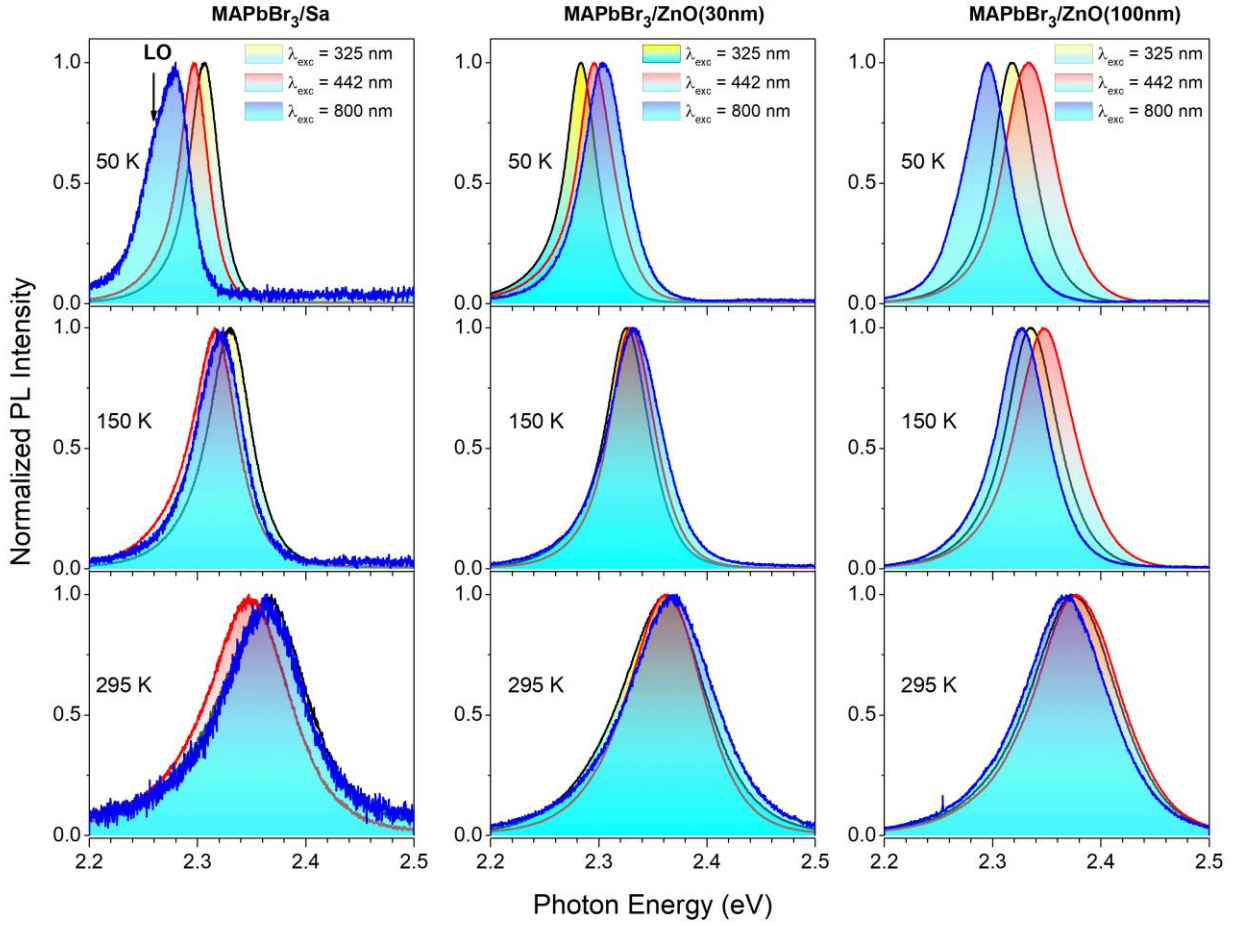


FIG. 4 PL spectra of the three samples, as indicated on the top of each of the columns, which were measured at the different excitation wavelengths, as indicated by the corresponding colors, and at different temperatures of 50, 150, and 296 K, as indicated for each of the panels.

between ~ 35 and ~ 90 meV, and (iv) the MAI-phonon modes and their combinations with averaged energy $\langle \hbar\omega_{MAI} \rangle$ ranging between ~ 100 and ~ 700 meV.

B. Structural phase transitions in 3D MAPbBr₃ nanocrystals

The structural phase transitions in MAPbX₃ have been monitored for single-crystal MAPbBr₃^{13-18,20,21} and MAPbI₃^{16,19,20} using the XRD,^{13,14,18} absorption,¹⁶ reflection,¹⁷ one-photon excited PL,^{13,14,18,19,21} two-photon excited PL,¹⁵ and dielectric response²⁰ techniques. Polycrystalline films,^{21,22,23} microplate crystals²⁴ and nanowires²⁵ of MAPbBr₃²³ and MAPbI₃²¹⁻²⁵ have also been studied using the XRD,²² absorption,^{21,23} charge transport²⁴ and one-photon excited PL^{21,22,24,25} techniques to recognize the structural phase transitions on the nanoscale. The structural phase transition in MAPbX₃ usually appears as the stepwise shift of the corresponding spectral band¹³⁻²⁵ whereas its intensity is less suitable for this purpose.^{18,19,21,22,24} Three structural phase transitions were found to occur at $T \sim 145$ K [orthorhombic(O)-to-tetragonal(T1)], at $T \sim 155$ K [tetragonal(T1)-to-tetragonal(T2)], and at $T \sim 237$ K [tetragonal(T2)-to-cubic(C)], which usually appear in single-crystal MAPbX₃ and its polycrystalline thin film.^{13,15} However, even a shift of the absorption and PL bands was incapable for recognizing the structural phase transition in MAPbX₃ nanocrystals.²¹ The reason that a stepwise shift of the absorption and PL bands is no longer observable in MAPbX₃ nanocrystals has been suggested

to arise from the configurational entropy loss upon suppressing long-range MA polar order.^{21,27,28}

To study the structural phase transition in a layer of 3D MAPbBr₃ nanocrystals, we measured the temperature dependences of PL from the aforementioned three samples using the three laser excitation regimes of photon energy (i) 3.81 eV ($\lambda_{exc} = 325$ nm) being above ZnO and MAPbBr₃ band gaps ($E_g = \sim 3.37$ and ~ 2.3 eV, respectively); (ii) 2.81 eV ($\lambda_{exc} = 442$ nm) being below ZnO band gap but above MAPbBr₃ band gap; (iii) 1.55 eV ($\lambda_{exc} = 800$ nm) being below ZnO and MAPbBr₃ band gaps [Fig. 1(b)]. Figure 3 shows PL spectra measured as a function of temperature using the three different laser excitations, as indicated for each of the panels. Additionally, Figure 4 shows PL spectra measured at temperatures $T = 50, 150,$ and 285 K, which correspond to the orthorhombic, tetragonal, and cubic structural phases of single-crystal MAPbBr₃, respectively. All PL spectra demonstrate a characteristic ≤ 100 meV blue-shift with increasing temperature from $T \sim 20$ to 295 K (Fig. 3 and Fig. 4). The position of PL peak in low-temperature spectra ($T = 50$ K) slightly vary with excitation photon energy in the range of $\sim 30 - 40$ meV. This variation sets up the range of inhomogeneous broadening, which is believed to be due to the nanocrystal structural imperfectness since the MAPbBr₃/ZnO heterointerface does not affect significantly the position of PL bands and their full width at half maximum (FWHM). Moreover,

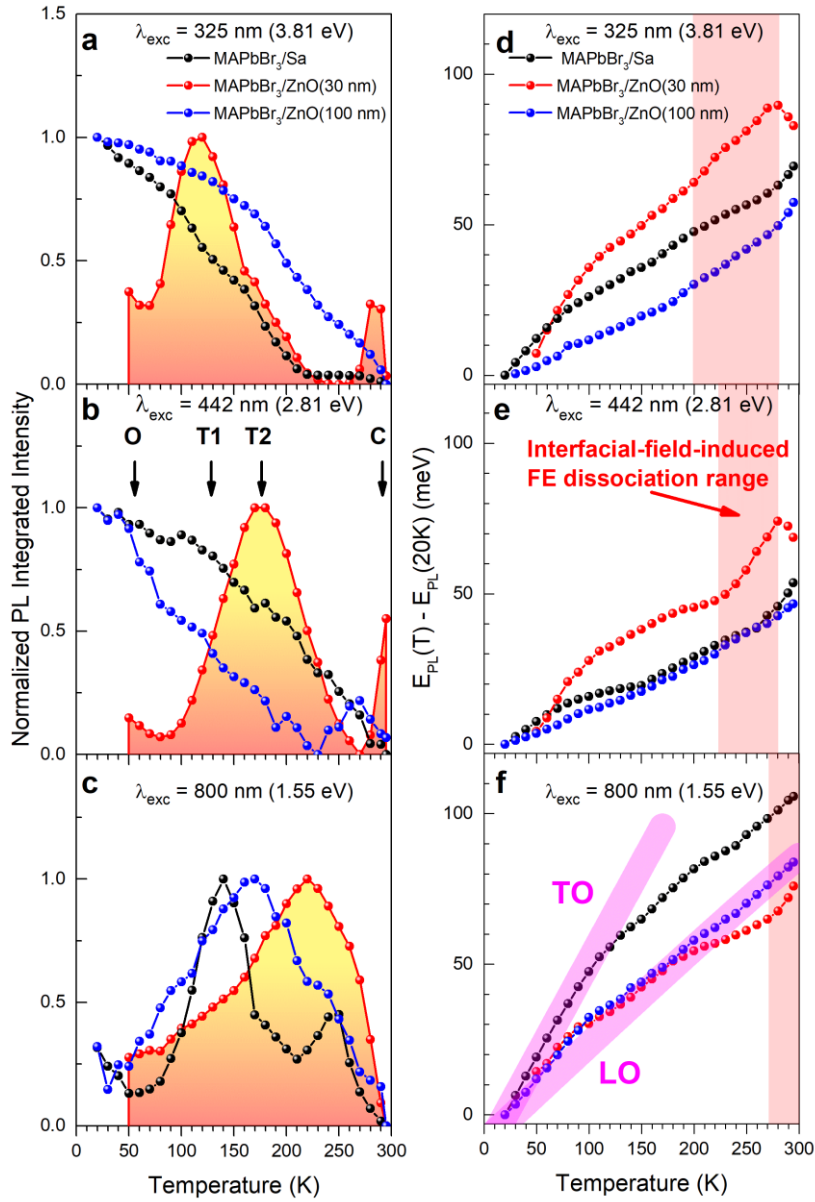


FIG. 5 (a), (b), (c) The normalized temperature dependences of integrated PL intensities measured with the three laser excitations λ_{exc} , as indicated for each of the panels, for the three samples, as indicated by the corresponding colors. The maximal interfacial electric field sample is highlighted by a yellow-red filling. (d), (e), (f) The corresponding temperature dependences of PL peak position plotted as $E_{\text{PL}}(T) - E_{\text{PL}}(20\text{K})$. The orthorhombic (O), tetragonal (T1 and T2), and cubic (C) structural phases are indicated by arrows in (b). The interfacial-field-induced FE dissociation ranges are marked in (d) – (f) as vertical light-red rectangles. The numerically simulated results obtained using Eq. (14) for TO and LO phonons are shown in (f).

the LO-phonon sideband⁴⁸ is red-shifted from PL peak by ~ 18 meV for the MAPbBr₃/Sa sample when two-photon excitation is applied ($\lambda_{\text{exc}} = 800 \text{ nm}$) (Fig. 4). As temperature increases, both the PL peak position variations and the LO-phonon sideband peak are masked by homogeneous broadening due to dominant carrier scattering with optical phonons. The bandwidth of the room-temperature PL bands (FWHM) reaches ~ 90 meV, indicating that homogeneous and inhomogeneous broadenings are somewhat comparable. The PL broadening dynamics with increasing temperature will be discussed in detail in the next section.

There are two general tendencies characterizing the temperature-dependent dynamics of one-photon-excited PL ($\lambda_{\text{exc}} = 325 \text{ nm}$ or 442 nm). Specifically, PL peak intensities [Fig. 3(a),

(b), (d), (e), (g), (h)] and PL band integrated intensities [Fig. 5(a) and (b)] both show either a monotonic decrease with increasing temperature from 20 to 295 K for the MAPbBr₃/Sa and MAPbBr₃/ZnO(100nm) samples or a non-monotonic trend maximizing at moderate temperatures for the MAPbBr₃/ZnO(30nm) sample. In contrast, all samples show non-monotonic trends for two-photon-excited PL ($\lambda_{\text{exc}} = 800 \text{ nm}$) [Fig. 3(c), (f), (i) and Fig. 5(c)]. As we mentioned above, all PL peak positions reveal a nearly monotonic blue-shift with increasing temperature [Fig. 5(d)-(f)]. However, this general tendency might also include an inflection point at $T \sim 80 \pm 30 \text{ K}$, most likely pointing to the two different processes being involved. The largest blue-shift is observed for two-photon-excited PL (~ 100 meV), indicating that the effect depends on the

photoexcited carrier density, since at least 10-fold higher carrier density was photoexcited in this case compared to one-photon-excited PL. The temperature dependences of PL peak position for the MAPbBr₃/ZnO(30nm) sample also demonstrate the minor features when approaching room temperatures [Fig. 5(d) - (f)], pointing to more complicated dynamics in this case. The fairly monotonic blue-shift with increasing temperature is well consistent with that reported for MAPbI₃ nanocrystals and suggested to provide evidence that MAPbI₃ nanocrystals do not undergo the bulk phase transitions.²¹ Alternatively, we show that although the temperature dependences of PL peak position reveal a fairly monotonic behaviour, the temperature dependences of PL intensity can be either monotonic or non-monotonic depending on the PL excitation regime applied.

Figure 5(a)-(c) clearly demonstrates this dual behaviour for the MAPbBr₃/Sa sample. Specifically, although one-photon-excited PL decays with increasing temperature nearly monotonic, there are two distinct peaks for two-photon-excited PL, the positions of which ($T \sim 140$ K and ~ 245 K) closely match those known for the orthorhombic-to-tetragonal and tetragonal-to-cubic phase transitions in single-crystal MAPbBr₃.¹³⁻²¹ The temperature dependences of the integrated PL intensity can be fitted using the multiple Mott equation,⁵⁰ which for one-photon-excited PL, takes into consideration phonon-assisted PL quenching in all the structural phases (three terms), as well as in the phase transition regions (two terms),

$$I_{PL}(T) = \sum_{i=1}^{j=5} \left(\frac{I_{PLi}(0)}{1+c_i e^{-E_{ai}/k_B T}} \right), \quad (1)$$

where $I_{PLi}(0)$ is PL intensity at $T = 0$ for each of the terms, c_i is the pre-exponential factors characterizing the relative probabilities of non-radiative decay, and E_{ai} is the corresponding activation energies. We note that all 5 terms in Eq. (1) are positive for one-photon-excited PL, thus characterizing the overall phonon-assisted PL quenching, while partial contributions from the specific components can be weakly recognized [Fig. 6(c)]. However, the situation changes dramatically when switching to two-photon excited PL. Consequently, phonon-assisted PL quenching in each of the structural phases (three positive terms) still contribute into the temperature-dependent dynamics, however, together with PL intensity increase when the structural phase changes towards the higher symmetry one (two negative terms) [Fig. 6(a) - (c)]. This observation demonstrates a higher sensitivity of the nonlinear absorption coefficient to the crystalline lattice symmetry and suggests that the specific phonon modes participate in the structural phase transitions⁵¹ similarly to PL non-radiative decay.⁵⁰ Consequently, temperature dependences of both one-photon-excited and two-photon-excited PL intensities can be fitted using the same c_i and E_{ai} parameters, nevertheless, the intensity $I_{PLi}(0)$ of two terms governing the structural phase transition dynamics change sign when switching to two-photon-excited PL. Specifically, PL quenching in the orthorhombic phase involves TO-phonons ($E_{a1} \sim 5$ meV). In contrast, PL quenching in the tetragonal/cubic phase involves MAI-phonons ($E_{a3} \sim 204$ meV, $E_{a5} \sim 413$ meV). The orthorhombic-to-tetragonal phase transition is a phonon-assisted process which occurs owing to MAT-phonon activation ($E_{a2} \sim 45$ meV) whereas the tetragonal-to-cubic phase transition involves MAI-phonons ($E_{a4} \sim 615$ meV). We note also that the orthorhombic-to-tetragonal structural phase transition in 3D MAPbBr₃ nanocrystals is spread out over the $T \sim 70 - 140$ K range, which

is believed to be due to the configurational entropy loss and the corresponding structural phase instability when, unlike in single-crystal MAPbX₃, free rotations of the MA ions are no longer restricted strongly by long-range polar order.^{27,28} The resulting local field fluctuations in MAPbX₃ nanocrystals and the liquid-like motion of MA cations¹ weaken and smooth distortions of PbX₆ octahedra which are responsible for the band-edge electronic transitions, thus eliminating the stepwise shift of the corresponding absorption and PL bands.

Although the temperature dependences of the integrated PL intensity for the MAPbBr₃/ZnO(100nm) sample are quite similar to those of the MAPbBr₃/Sa sample, they differ significantly for the MAPbBr₃/ZnO(30nm) sample [Fig. 5(a)-(c)]. The dynamics can be associated with that being caused by the interfacial electric field.¹⁹ Specifically, one should distinguish between the two principally different PL excitation regimes. One of them ($\lambda_{exc} = 325$ nm) deals with the excitation of carriers in both MAPbBr₃ and ZnO. The charge separation process at the MAPbBr₃/ZnO heterointerface in this case is not efficient enough because although the photoexcited holes in both materials tend to reside in MAPbBr₃, the majority of photoexcited electrons in MAPbBr₃ do not leave it since the edge of the ZnO CB is filled by electrons photoexcited in ZnO [Fig. 1(b)]. The second regime involves the excitation of carriers exclusively in MAPbBr₃ ($\lambda_{exc} = 442$ and 800 nm) and hence the interfacial electric field at the MAPbBr₃/ZnO heterointerface is formed with high efficiency since electrons can freely move to the CB of ZnO whereas holes remain in MAPbBr₃ [Fig. 1(b)]. One can hence vary the strength of the interfacial electric field by varying the photoexcited carrier density and λ_{exc} .

The thickness of the ZnO layer also significantly affects the interfacial electric field strength. Specifically, the interfacial electric field in the MAPbBr₃/ZnO(30nm) sample is expected to be much stronger compared to that in the MAPbBr₃/ZnO(100nm) one. This statement can be clarified in the framework of the two effects that can potentially occur at the MAPbBr₃/ZnO heterointerface: (i) the strain-induced effect and (ii) the charge-separation-induced effect. The first one takes into consideration that the ZnO layer was grown on the sapphire substrate and hence the thicker the ZnO layer, the stronger the residual strain should act on MAPbBr₃ nanocrystals.⁵¹ The second effect also depends on the ZnO layer thickness, but in the opposite way. Because the strength of the interfacial electric field is proportional to the carrier density separated at the MAPbBr₃/ZnO heterointerface, the thicker the ZnO layer, the lower the carrier density in it and hence the weaker the interfacial electric field. This principal difference between the strain and electric field induced effects can be distinguished by testing two samples of different ZnO layer thicknesses, as it has been done in the current study. Specifically, the non-monotonic behaviour observed for the MAPbBr₃/ZnO(30nm) sample with one-photon excitation ($\lambda_{exc} = 325$ and 442 nm) points to the stronger interfacial electric field being involved in this sample. Moreover, as the strength of the interfacial electric field increases ($\lambda_{exc} = 442$ nm), the shift of the structural phase transition towards the higher temperature range also progresses. Alternatively, the temperature dependences of the MAPbBr₃/Sa and MAPbBr₃/ZnO(100nm) samples demonstrate a similar monotonic behaviour, suggesting that the interfacial electric field in MAPbBr₃/ZnO(100nm) sample is as weak as that in the MAPbBr₃/Sa sample and proving that the strain-induced effect is negligible [Fig. 5(a) and (b)]. This tendency is also confirmed

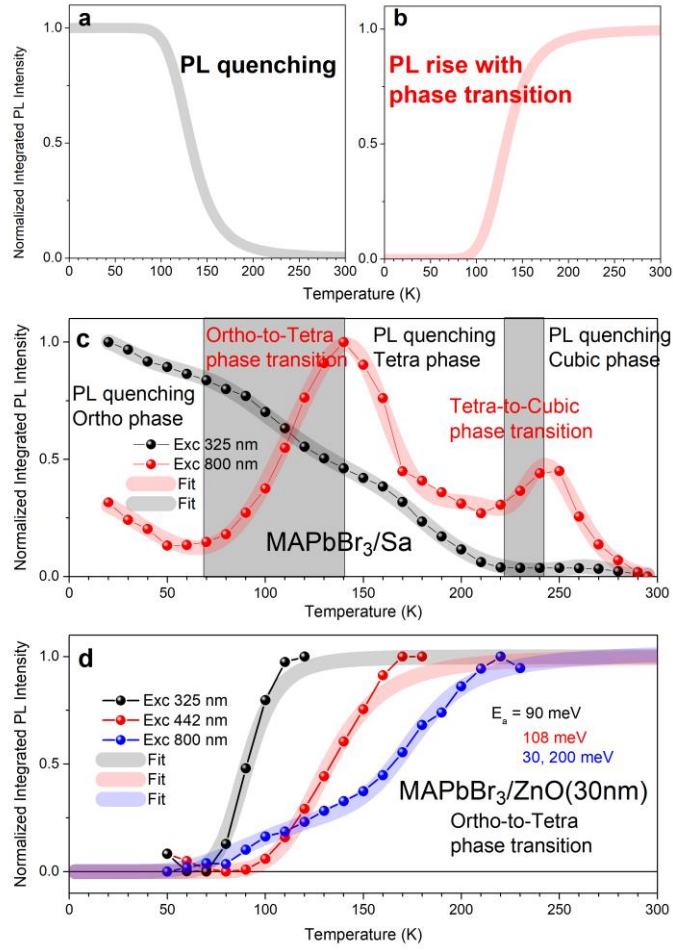


FIG. 6 (a) An example of the phonon-assisted PL quenching. (b) An example of the phonon-assisted structural phase transition presented using the Mott equation with negative amplitude. (c) The multiple Mott equation fit of the temperature dependences of the PL integrated intensity of the MAPbBr₃/Sa sample measured in the one-photon and two-photon excitation regimes. The ranges of PL quenching in different structural phases and the structural phase transitions are indicated. (d) The orthorhombic-to-tetragonal structural phase transition range and its extension towards the higher temperatures for different excitation regimes in the MAPbBr₃/ZnO(30nm) sample, as indicated by the corresponding colors. To fit experimental curves, the Mott equation with negative amplitude was used. The corresponding activation energies are listed.

using two-photon-excited PL ($\lambda_{\text{exc}} = 800$ nm), despite the non-monotonic temperature dependences for all the samples.

Specifically, the temperature dependence of two photon-excited PL intensity for the MAPbBr₃/ZnO(100-nm) sample looks more like that for the MAPbBr₃/Sa sample [Fig. 5(c)].

The orthorhombic-to-tetragonal phase transition in the MAPbBr₃/ZnO(30nm) sample reaches the extremely broad temperature range of $T \sim 70 - 230$ K [Fig. 5(a)-(c) and Fig. 6(d)], confirming once again that the interfacial electric field in this sample is enhanced. The dynamics also demonstrate more clearly the existence of T1 and T2 subphases. The corresponding activation energies are in the range of MAT- and MAI-phonons [Fig. 6(d)], confirming that the structural phase instability results from the MA dipole order suppression. Additionally, if the $\lambda_{\text{exc}} = 800$ nm excitation regime is applied, the cubic structural phase feature is not observed for the MAPbBr₃/ZnO(30nm) sample even for temperatures ranging up to $T \sim 295$ K [Fig. 5(a)-(c)], suggesting that the room-temperature structural phase in this case most likely is also unstable, being the mixture of the orthorhombic and tetragonal phases.

To estimate how far the interfacial electric field is extended inward towards the MAPbBr₃ nanocrystal core, we calculated the Thomas-Fermi screening length for the photoexcited carrier densities $n_c = 1.0 \times 10^{19} \text{ cm}^{-3}$, $n_c = 1.0 \times 10^{18} \text{ cm}^{-3}$ and $n_c = 1.0 \times 10^{17} \text{ cm}^{-3}$ (see the Experimental Methods section) as $1/k_{TF} \sim 2.7 \text{ nm}$, $\sim 3.9 \text{ nm}$ and $\sim 5.8 \text{ nm}$, respectively, with k_{TF} being the Thomas-Fermi wavevector defined as $k_{TF}^2 = \left(\frac{3}{\pi^4}\right)^{1/3} \frac{m_c^* e^2 n_c^{1/3}}{\epsilon_s \epsilon_0 \hbar^2}$,^{19,53} where m_c^* is the carrier effective mass ($m_e^* = 0.13m_0$ and $m_h^* = 0.19m_0$ for electrons and holes, respectively, with m_0 being the free-electron mass), e is the electron charge, $\epsilon_s = 21.36$ is the static dielectric constant, and ϵ_0 is the permittivity of free space.⁹ Consequently, the Thomas-Fermi screening length naturally decreases with increasing carrier density, indicating that the interfacial electric field tends self-consistently to be confined at the heterointerface when the photoexcited carrier density increases. Because the range of the orthorhombic-to-tetragonal structural phase transition also extends with increasing photoexcited carrier density, the latter behaviour implies that the strength of the interfacial electric field mainly governs the

structural phase instability in the whole MAPbBr₃ nanocrystal rather than the field extension inward towards the nanocrystal core. The short-range Thomas-Fermi screening length also suggests that the long-range MA dipole order which was suppressed substantially in the whole MAPbBr₃ nanocrystal cannot be restored by the interfacial electric field.

We also note that the temperature dependences of PL peak position observed for the MAPbBr₃/ZnO(30nm) sample demonstrate some additional features when approaching room temperature [Fig. 5(d) - (f)]. We associate these features with FE dissociation because of stronger interfacial electric field in this sample.¹⁹ Specifically, the interfacial electric field dissociates FEs in the tetragonal phase, giving rise to the blue-shift of the PL band because of progressive switching from FE to band-to-band recombination. The rate of this process strongly depends on the electric field strength, thus being maximised for the $\lambda_{exc} = 442$ nm and $\lambda_{exc} = 800$ nm excitation regimes. Once the tetragonal-to-cubic structural phase transition occurs, the FE dissociation process weakens, giving rise to the red-shift of the PL band since FE binding energy in the cubic structural phase is higher compared to that in the tetragonal phase.⁵⁴ It should be noted that applying $\lambda_{exc} = 800$ nm excitation, one can observe only the initial blue-shift of the PL band because the tetragonal-to-cubic structural phase transition in this case occurs at temperatures higher than room temperature [Fig. 5(f)].

C. PL excitation mechanisms

The formation of the interfacial electric field of different strengths is also one of the key circumstances of why PL technique becomes sensitive enough to negligible structural distortions in 3D MAPbBr₃ nanocrystals. Specifically, this behaviour is realized because PL excitation involves the absorption rates governed by the second-order and third-order nonlinear susceptibilities, which owing to their higher rank tensor nature compared to the first-order susceptibilities, are known to demonstrate a higher spatial sensitivity to the lattice symmetry.⁵⁵⁻⁵⁸ The situation emerging is known as electric-field-induced one-photon-excited PL and two-photon-excited PL, both involving nonlinear susceptibilities.⁵⁵ This behaviour is in stark contrast to the conventional one-photon-excited PL which loses sensitivity to the structural phase transition in 3D MAPbX₃ nanocrystals because of structural phase instability and the corresponding negligible distortions of PbX₆ octahedra responsible for light-emitting process. It is worth noting that all three structural phases in MAPbX₃ materials are centrosymmetric.^{59,60} This statement significantly distinguishes between PL excitation regimes through the light absorption rate. Specifically, PL intensity can be expressed as⁶¹

$$I_{PL} \propto R_{em} \quad , \quad (2)$$

where $R_{em} \propto n_e n_h$ is the emission rate caused by carrier radiative recombination with n_e and n_h being the density of electrons and holes, respectively. The latter process is known as bimolecular recombination and mainly appears through electroluminescence (EL), when n_e and n_h , in general, can be different as a consequence of the specific structure of the samples, their doping type, as well as the carrier injection level. Additionally, for highly efficient light-emitters, n_e and n_h should be low enough to guarantee the carrier wavevector conservation in the recombination process.⁶¹

In contrast, in PL experiments one always excites equal numbers of electrons and holes, $n = n_e = n_h$ (each photon with energy exceeding band gap energy excites two particles, electron and hole), with energies equal to one half of the difference between photon and band gap energies. The density of photoexcited carrier is usually much higher compared to the intrinsic carrier density (the doping level). Furthermore, PL resulting from recombination between nonthermalized (hot) carriers (hot PL) should also be negligible since the wavevector is not strictly conserved for them. However, if wavevector conservation is not necessary, the situation which may happen due to the trapping of carriers by defects or carrier interaction with phonons (including the polaron formation as well), the rate $R_{em} \propto n$ (monomolecular recombination) if the photoexcited carrier density exceeds the intrinsic carrier density.⁶¹ The latter proportionality indicates that two-particle recombination is a highly probable process emitting a single photon. The monomolecular recombination is hence a direct opposite of the PL excitation process and its rate is known to be significantly enhanced as compared to that of bimolecular recombination.⁶¹ Because $n \propto R_{abs} R_{rel}$, where R_{abs} and R_{rel} are rates of light absorption and carrier relaxation to the light-emitting states, respectively,⁶¹ and because R_{rel} is expected to be a constant for the fixed incident photon energy, as that occurs in our case, PL intensity can be expressed as

$$I_{PL} \propto R_{abs}, \quad (3)$$

that is, being predominantly governed by the absorption rate R_{abs} (in units of s⁻¹), which, in general, is a sum of several contributions associated with one-photon absorption $R_{abs}^{(1)}$, two-photon absorption $R_{abs}^{(2)}$ if the excitation light intensity (I_{exc}) is strong enough, and one-photon electroabsorption $R_{eabs}^{(1)}$ if an external or internal electric field is applied, so that

$$R_{abs} = R_{abs}^{(1)} + R_{eabs}^{(1)} + R_{abs}^{(2)} = \frac{I_{exc}}{\hbar\omega_{exc}} \left\{ [\sigma_{abs}^{(1)} + \sigma_{eabs}^{(1)}] + \frac{I_{exc}}{\hbar\omega_{exc}} \sigma_{abs}^{(2)} \right\}, \quad (4)$$

where $\hbar\omega_{exc}$ is the excitation photon energy, $\sigma_{abs}^{(1)}$, $\sigma_{eabs}^{(1)}$ and $\sigma_{abs}^{(2)}$ are the corresponding one-photon and two-photon cross sections.⁵⁵ If $\hbar\omega_{exc} > E_g$, then the $R_{abs}^{(1)}$ and $R_{eabs}^{(1)}$ terms dominate the PL excitation dynamics. On the contrary, if $\hbar\omega_{exc} < E_g$, then the $R_{abs}^{(2)}$ term completely governs the PL excitation mechanism. Consequently, the following proportionalities $I_{PL} \sim I_{exc}$ and $I_{PL} \sim I_{exc}^2$ correspond to one-photon-excited and two-photon-excited PL, respectively.⁶²⁻⁶⁵ These relations can be confirmed experimentally when analyzing the slope of the power dependences of I_{PL} presented in a log-log plot (Fig. 7).

However, the absorption rates of the one-photon and two-photon absorption processes are known to be proportional to the imaginary part of the first-order and third-order optical susceptibilities ($\sigma_{abs}^{(1)} \sim \text{Im}[\chi^{(1)}]$ and $\sigma_{abs}^{(2)} \sim \text{Im}[\chi^{(3)}]$), respectively.⁵⁵ Consequently, this approach is well consistent with the aforementioned centrosymmetry restriction applied to MAPbBr₃ crystals, according to which the second-order nonlinear process [$\chi^{(2)}$] is not allowed, whereas the linear [$\chi^{(1)}(-\omega; \omega)$] and third-order nonlinear [$\chi^{(3)}(-\omega; \omega, \omega, -\omega)$] processes should completely govern the one-photon and two-

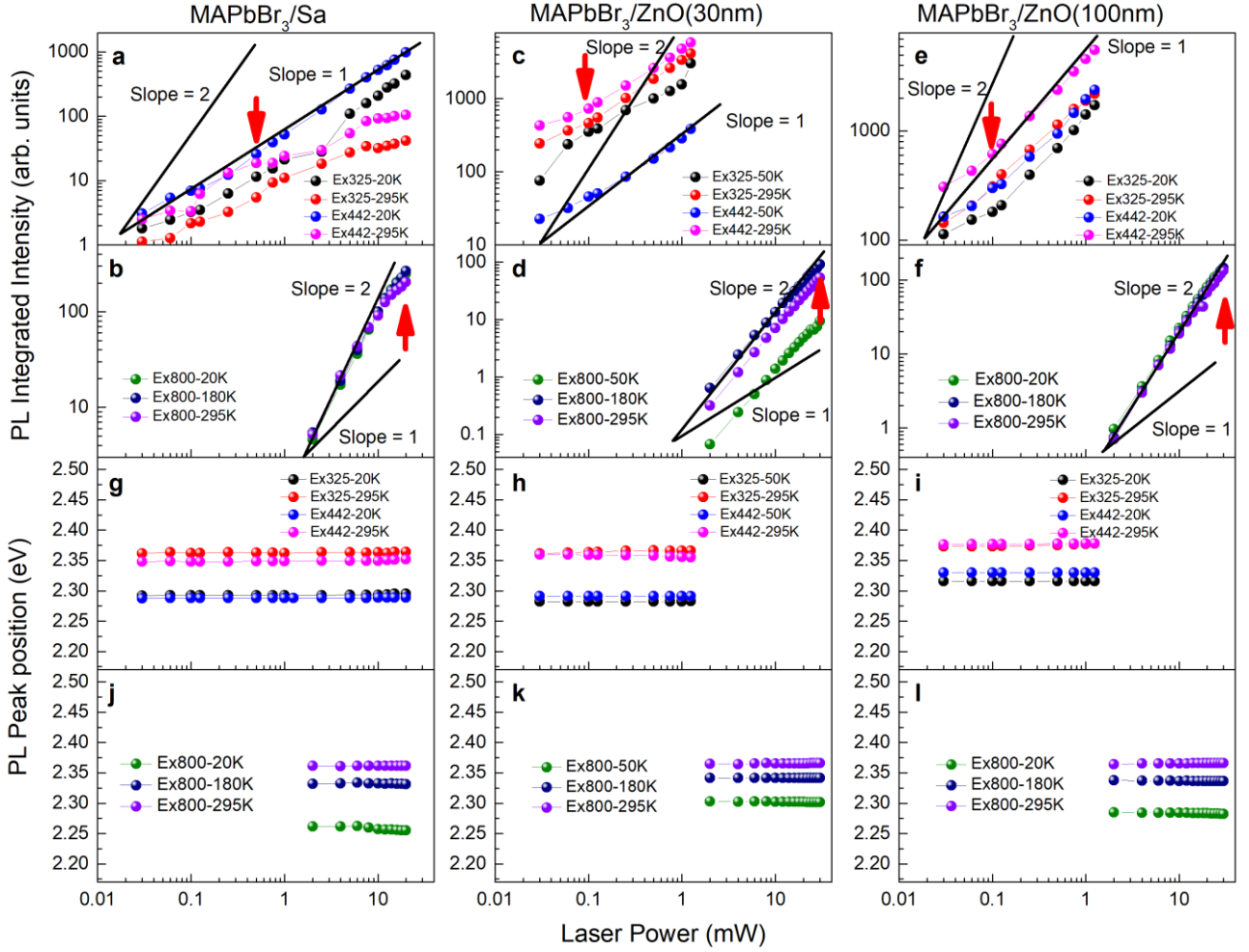


FIG. 7 (a)-(f) Power dependences of the integrated PL intensity presented in the log-log scale for the three samples, as indicated at the top, which were measured at different temperatures and excitations, as indicated by the corresponding colors. The slopes of the rise of the integrated PL intensity with increasing laser power indicate the one-photon and two-photon excitation regimes. The red vertical arrows mark average powers at which the temperature-dependent PL measurements were performed. (g)-(l) Power dependences of PL-peak position presented in the semi-log scale for the same three samples, which demonstrate no significant effect on the PL-peak position, confirming hence high resistance of a fully encapsulated layer of 3D MAPbBr₃ nanocrystals against light exposure.

photon absorption in these materials, appearing through one-photon-excited and two-photon-excited PL, respectively. However, once the crystalline lattice is getting distorted by an external or internal electric field, for example, the centrosymmetry breaking allows the second-order nonlinear process to appear through the linear electro-optic effect $\sigma_{eabs}^{(1)} \sim Im[\chi^{(2)}(-\omega; \omega, 0)]$ (Franz-Keldysh effect).^{55-58,61} Additionally, the electric field can induce a quadratic electro-optic effect $\sigma_{eabs}^{(1)} \sim Im[\chi^{(3)}(-\omega; \omega, 0, 0)]$ (Kerr effect).⁵⁵⁻⁵⁸ We note that PL excitation involving $\chi^{(2)}(-\omega; \omega, 0)$ and $\chi^{(3)}(-\omega; \omega, 0, 0)$ still produces a one-photon-excited PL response, although the light absorption rates are characterized by nonlinear electro-optic susceptibilities. This brief discussion of nonlinear optics highlights an advantage of the electric-field-induced one-photon-excited and two-photon-excited PL for monitoring structural phase transitions in hybrid perovskite nanoscale materials. This behaviour results from the fact that these techniques exploit the higher sensitivity of nonlinear optical and electro-optical susceptibilities to the crystalline lattice distortions compared to the conventional linear optical

processes.⁵⁵⁻⁵⁸ Specifically, $\chi^{(1)}(-\omega; \omega)$ is a second rank tensor containing 9 elements, whereas $\chi^{(2)}(-\omega; \omega, 0)$ and $\chi^{(3)}(-\omega; \omega, 0, 0)$, $\chi^{(3)}(-\omega; \omega, \omega, -\omega)$ are the third and fourth rank tensors containing 27 and 81 elements, respectively.⁵⁵ This principal difference also indicates that both $R_{eabs}^{(1)}$ and $R_{abs}^{(2)}$ mainly characterize PL excitation in the nanocrystal core, contrary to $R_{abs}^{(1)}$ which characterizes PL excitation in both the nanocrystal core and the nanocrystal surface. Consequently, because the ratio of the surface-to-core PL contributions for nanocrystals is large enough and because the surface states are less sensitive to the structural phase transitions in the core, the structural phase transitions in MAPbX₃ nanocrystals can be significantly masked by PL from the surface states when conventional one-photon excitation is applied. This circumstance together with the structural phase instability occurring within the broad temperature range seems to be a reason why the structural phase transitions in MAPbX₃ nanocrystals have never been observed.

It is worth noting that PL peak position remains almost unchanged with increasing laser power for all the samples and

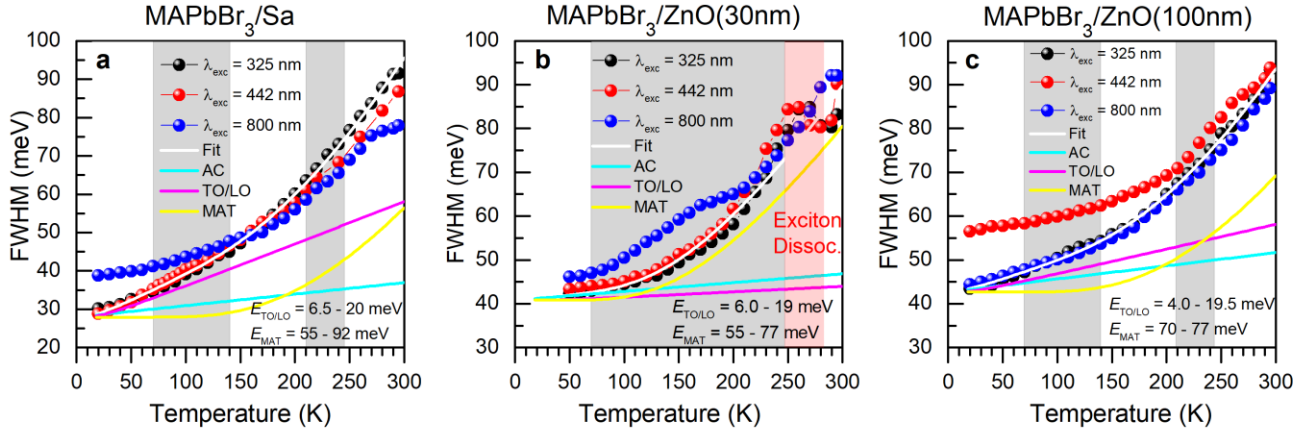


FIG. 8 (a)-(c) The temperature dependences of the PL band FWHM measured at the three laser excitations λ_{exc} , as indicated by the corresponding colors. An example of the fit using Eq. (5) is shown for PL measured with $\lambda_{\text{exc}} = 325$ nm, where acoustic phonon (AC), TO/LO-phonon, and MAT-phonon modes were taken into consideration. The corresponding components of the fit and the estimated ranges of the averaged phonon energies are shown. The light-gray color filled rectangles show the structural phase transition ranges defined in Fig. 6(c) and (d). The light-red color filled rectangle in (b) show the FE dissociation range for MAPbBr₃/ZnO(30nm) when $\lambda_{\text{exc}} = 325$ nm or $\lambda_{\text{exc}} = 442$ nm excitation is applied (narrowing PL band).

all the structural phases [Fig. 7(g)-(l)], thus eliminating from consideration any laser-induced sample modification effects.

D. PL broadening dynamics

To gain deeper understanding through the phonon-assisted structural phase transitions in 3D MAPbBr₃ nanocrystals, the temperature dependences of the PL band FWHM for all the samples were analysed (Fig. 8). All the dependences clearly demonstrate the two-stage homogeneous broadening process appearing at low ($T \sim 20 - 140$ K) and moderate ($T \sim 140 - 295$ K) temperatures. These two temperature intervals closely match those corresponding to the orthorhombic and tetragonal-cubic phases in single-crystal MAPbBr₃, respectively. However, PL broadening dynamics with temperature is expected to be governed rather by various phonons being involved than the structural phase transitions. The temperature dependences of the PL band FWHM also reveal additional features for the MAPbBr₃/ZnO(30nm) sample when approaching room temperature. These features are due to the interfacial-field-induced FE dissociation, which additionally to the blue-shift of the PL band [Fig. 5(d) – (f)] is accompanied by its narrowing.¹⁹ Further broadening of the PL band with increasing temperature occurs when the tetragonal phase transforms to the cubic one, at which FE binding energy is increased and hence the FE dissociation process is slowed down, as discussed in the preceding section for the PL peak position dynamics.

To analyze the PL band FWHM variations with temperature, we use a phenomenological approximation for phonon-induced broadening^{19,66,67}

$$\gamma = \gamma_0 + \gamma_{ac}T + \frac{\gamma_{\text{TO/LO}}}{\exp\left(\frac{\hbar\omega_{\text{TO/LO}}}{k_B T}\right) - 1} + \frac{\gamma_{\text{MAT}}}{\exp\left(\frac{\hbar\omega_{\text{MAT}}}{k_B T}\right) - 1}, \quad (5)$$

where γ_0 is inhomogeneous broadening, γ_{ac} is the electron (hole)-acoustic-phonon coupling strength, $\gamma_{\text{TO/LO}}$ is the electron (hole)-TO/LO-phonon coupling strength, γ_{MAT} is the electron (hole)-MAT-phonon coupling strength. Consequently, the electron (hole)-acoustic-phonon coupling strength ($\gamma_{ac} \sim 3 \times 10^{-5}$ eV K⁻¹) is negligible [Fig. 8(a)-(c)], being of the same order as that

previously reported.^{19,66} The first stage of PL band broadening is due to the scattering of carriers with TO/LO-phonons, whereas the second stage can be attributed to the MAT-phonons effect. It should be especially stressed here that the MAT-phonon contribution becomes significantly enhanced for the MAPbBr₃/ZnO(30nm) sample [Fig. 8(b)]. This behaviour confirms the stronger interfacial electric field in this sample to occur and its significant effect on the suppression of the MA cation dipole order in the whole nanocrystal.⁴⁵ We note that the fits are not necessarily unique, thus allowing one to determine the effective energy ranges of TO/LO-phonons as $\langle \hbar\omega_{\text{LO/TO}} \rangle \sim 4.0 - 17$ meV and MAT-phonons as $\langle \hbar\omega_{\text{MAT}} \rangle \sim 55 - 92$ meV, which well match those discussed above in the sample characterization section.

We also found that the electron (hole)-MAT-phonon coupling strength ($\gamma_{\text{MAT}} \sim 245 - 679$ meV) is ~ 100 -fold greater than the electron (hole)-TO/LO-phonon coupling strengths ($\gamma_{\text{TO/LO}} \sim 2.5 - 8.4$ meV). This strong coupling of electrons (holes) to MAT-phonons highlights the main specific feature distinguishing the carrier relaxation in MAPbX₃ compared to conventional semiconductors. Specifically, the photoexcited carriers relax down not only through the TO/LO-phonon cascade, but also through the MAT-phonon excitation. This behaviour is the reason why TO/LO-phonon bottleneck occurs in MAPbX₃. Specifically, because of the ultralow thermal conductivity between the sublattices, the organic sublattice heated during carrier relaxation keeps TO/LO-phonons in the inorganic sublattice at the temperature of the former, thus blocking their decay through acoustic phonons (Klemens-Ridley anharmonic process) and allowing carriers to reabsorb TO/LO-phonons.²⁻⁴ This process is expected to be enhanced in nanocrystals as a consequence the additional reduction of thermal conductivity through the nanocrystal boundaries. Consequently, the nearly monotonic blue shift of PL band with increasing temperature seems to result rather from the heating effect under TO/LO-phonon bottleneck than that being induced by a progressive distortion of PbX₆ octahedra. This conclusion is also well consistent with the structural phase instability in

MAPbX₃ nanocrystals due to the configurational entropy loss.^{21,27,28}

E. PL mechanism

PL mechanism in MAPbX₃ is not trivial mainly due to a polar crystal lattice and the ultralow thermal conductivity between the sublattices. The observed dominant PL blue-shift with increasing lattice temperature (T) [Fig. 5(d)-(f)] is opposite to that usually predicting the band gap (E_g) variation in conventional semiconductors^{61,68,69}

$$E_g(T) = a - b \left[1 + \frac{2}{\exp(\frac{\theta}{T}) - 1} \right], \quad (6)$$

where a and b are fitting parameters and θ is the mean temperature of phonons taking part in the scattering process with carriers. It has recently been suggested that $E_g(T)$ can show either a decrease (red-shift) or an increase (blue-shift) depending on whether derivative $d\theta/dT$ (slope) is positive (phonon emission) or negative (phonon reabsorption), respectively.¹⁸ The latter behavior points to the non-equilibrium dynamics, being equivalent to the introduction of the negative absolute temperature.⁷⁰

To adapt this situation to TO/LO-phonon bottleneck, we consider the Bose–Einstein phonon occupation numbers for spontaneous TO/LO-phonon emission

$$n_{em} = \left[\exp(\langle \hbar\omega_{\text{TO/LO}} \rangle / k_B T) - 1 \right]^{-1} \quad (7)$$

and for TO/LO-phonon reabsorption

$$n_{ra} = \left\{ \exp[\langle \hbar\omega_{\text{TO/LO}} \rangle / k_B (T_b - T)] - 1 \right\}^{-1}, \quad (8)$$

where T_b denote the temperature at which TO/LO-phonon bottleneck occurs. This approach implies that upon photoexcitation, electrons and holes (also FEs) cool down through the TO/LO/MAT-phonon cascade. Consequently, free carriers and FEs relax down at least within a few ps timescale and their temperature in the light-emitting states prior to emission (T_e) is determined by the decay of TO/LO-phonons in the inorganic sublattice through the Klemens-Ridley anharmonic process^{2-4,30,31}, which however is controlled by the organic sublattice temperature (T_b). Because the further cooling of the organic sublattice through acoustic phonons is slower than that of the inorganic sublattice due to the more energetic optical phonons involved in the organic sublattice, TO/LO-phonon bottleneck in the inorganic sublattice occurs at $T_e = T_b > T$ and allows carriers in the latter to reabsorb TO/LO-phonons. The effect progresses with increasing T , since the organic sublattice cooling rate is reduced. Consequently, TO-phonon bottleneck occurs predominantly in the orthorhombic phase whereas LO-phonon bottleneck dominates in the tetragonal/cubic phase. The resulting TO/LO-phonon-dressing process hence lowers the electron (hole, exciton) energies by the polaron (reorganization) energy^{1,7,10,71-73}. Consequently, the stronger the electron (hole, exciton)-phonon coupling, the larger the number of TO/LO-phonons contribute to the polaronic effect.

According to this model, the resulting polaronic electron (pe), polaronic hole (ph) and polaronic exciton (PE) quasiparticles are involved into their further recombination in MAPbBr₃ nanocrystals, thus completely governing their PL and

transport properties. Moreover, upon TO/LO-phonon bottleneck, polaronic quasiparticles can reabsorb TO/LO-phonons to form the TO/LO-phonon vibrationally excited polaronic quasiparticles with reduced ground-state polaron energy. Consequently, polaronic quasiparticle recombination may occur in either the ground or vibrationally excited polaron states [Fig. 9(a)]. This behavior gives rise to the ~ 100 meV blue-shift of PL-peak with increasing temperature, unlike a red-shift in conventional semiconductors. Because the blue-shift is observed for the entire temperature range applied, one can assume that $T_b > 300$ K whereas it should apparently be less than the material melting point of $T_b < 450$ K. Owing to screening from other carriers and defects, polaronic quasiparticles possess a very small recombination rate (PL decay-time is very long), thus being expected to demonstrate high mobility and long-range diffusion.

To treat the experimental results, we first consider the single electron (hole) polaron energy. The polaronic band gap renormalization is known to narrow the band gap by reorganization energy, introducing the ground-state Fröhlich polaron energy for electrons and holes which can be given as^{71,74}

$$\lambda_{e,h} = \langle \hbar\omega_{\text{TO/LO}} \rangle \langle \alpha_{e,h} \rangle, \quad (9)$$

where $\langle \alpha_{e,h} \rangle = \frac{e^2}{\hbar} \frac{1}{4\pi\epsilon_0} \sqrt{\frac{m_{e,h}^*}{2\langle \hbar\omega_{\text{TO/LO}} \rangle}} \left(\frac{1}{\epsilon_\infty} - \frac{1}{\epsilon_s} \right)$ is the pe/ph coupling coefficient which is a measure of electron(hole)-phonon coupling strength^{9,74,75}. Using $\langle \hbar\omega_{\text{TO}} \rangle = 5$ meV and $\langle \hbar\omega_{\text{LO}} \rangle = 18.6$ meV, one can obtain the following Fröhlich polaron coupling coefficients $\langle \alpha_e \rangle = 3.37$, $\langle \alpha_h \rangle = 4.07$ and $\langle \alpha_e \rangle = 1.75$, $\langle \alpha_h \rangle = 2.11$ for TO and LO phonons, respectively, which are well consistent with those calculated using the Feynman-Osaka model⁹. The ground-state Fröhlich polaron energy for electrons and holes is hence temperature independent and can be calculated as $\lambda_e = \sim 16.9$ meV and $\lambda_h = \sim 20.35$ meV for TO-phonons and $\lambda_e = \sim 32.6$ meV and $\lambda_h = \sim 39.2$ meV for LO-phonons. These estimates imply that LO-phonons might govern the room-temperature ~ 60 meV Stokes shift ($\lambda_e + \lambda_h$) discussed above in the sample characterization section. Specifically, assuming that the absorption and PL spectra manifest the unperturbed and BGR-induced dynamics, respectively, the corresponding band gap narrowing is

$$E_g^{BGR} = E_g - (\lambda_e + \lambda_h) \quad (10)$$

and the Stokes shift is hence equal to $\lambda_e + \lambda_h$. To introduce the temperature effect into the dynamics, we use the Bose–Einstein phonon occupation numbers defined above, so that

$$\lambda_{e,h} = \langle \hbar\omega_{\text{TO/LO}} \rangle \langle \alpha_{e,h} \rangle [n_{em} + n_{ra}] = \frac{1}{2} \langle \hbar\omega_{\text{TO/LO}} \rangle \langle \alpha_{e,h} \rangle \left\{ \coth \left(\frac{\langle \hbar\omega_{\text{TO/LO}} \rangle}{2k_B T} \right) + \coth \left[\frac{\langle \hbar\omega_{\text{TO/LO}} \rangle}{2k_B (T_b - T)} \right] - 2 \right\}. \quad (11)$$

The corresponding variation of the band gap afterwards is

$$E_g^{BGR}(T) = E_g(0) - \frac{1}{2} \langle \hbar\omega_{\text{TO/LO}} \rangle (\langle \alpha_e \rangle + \langle \alpha_h \rangle) \times \left\{ \coth \left(\frac{\langle \hbar\omega_{\text{TO/LO}} \rangle}{2k_B T} \right) + \coth \left[\frac{\langle \hbar\omega_{\text{TO/LO}} \rangle}{2k_B (T_b - T)} \right] - 2 \right\} \quad (12)$$

We note that when neglecting TO/LO-phonon reabsorption term ($n_{ra} = 0$), Eq. (12) is reduced to the standard hyperbolic cotangent equation derived on the basis of simple

thermodynamics to replace the semi-empirical Varshni relation,⁷⁶

$$E_g^{BGR}(T) = E_g(0) - \frac{1}{2} \langle \hbar \omega_{\text{TO/LO}} \rangle (\langle \alpha_e \rangle + \langle \alpha_h \rangle) \times \left\{ \coth \left(\frac{\langle \hbar \omega_{\text{TO/LO}} \rangle}{2k_B T} \right) - 1 \right\}. \quad (13)$$

Alternatively, when neglecting spontaneous TO/LO-phonon emission term ($n_{em} = 0$), Eq. (12) describes an increase of the band gap with temperature

$$E_g^{BGR}(T) = E_g(0) - \frac{1}{2} \langle \hbar \omega_{\text{TO/LO}} \rangle (\langle \alpha_e \rangle + \langle \alpha_h \rangle) \times \left\{ \coth \left[\frac{\langle \hbar \omega_{\text{TO/LO}} \rangle}{2k_B (T_b - T)} \right] - 1 \right\}. \quad (14)$$

We note that Eq. (12) completely describes the variation of the polaronic band gap energy of MAPbX₃ nanocrystals, depending on whether TO/LO-phonon bottleneck occurs. To use this approach to *PEs*, one should consider the *PE* binding energy $\varepsilon_{PE} \equiv E_{g.s.} - \lambda_e - \lambda_h$, where $E_{g.s.}$ is the *PE* ground-state energy [Fig. 9(a)].⁷⁷ Because ε_{PE} for MAPbBr₃ is similar to the exciton binding energy ($\varepsilon_{PE} \approx \varepsilon_{ex}$) and because $\varepsilon_{PE} = 35$ meV is higher than the room temperature $k_B T = 25.7$ meV,^{16,77} we consider *PEs* as those dominantly contributing to PL in the temperature range of 20 - 295 K. Consequently, the exciton peak energy in absorption and PL spectra varies as follows

$$\begin{aligned} E_{ex}(T_L) &= E_g(0) - E_{g.s.} \\ &= E_g(0) - \varepsilon_{PE} - \frac{1}{2} \langle \hbar \omega_{\text{TO/LO}} \rangle (\langle \alpha_e \rangle + \langle \alpha_h \rangle) \\ &\times \left\{ \coth \left(\frac{\langle \hbar \omega_{\text{TO/LO}} \rangle}{2k_B T} \right) + \coth \left[\frac{\langle \hbar \omega_{\text{TO/LO}} \rangle}{2k_B (T_b - T)} \right] - 2 \right\}. \end{aligned} \quad (15)$$

Accordingly, the $\coth \left[\frac{\langle \hbar \omega_{\text{TO/LO}} \rangle}{2k_B (T_b - T)} \right]$ term characterizing the non-equilibrium dynamics and governing the blue shift with temperature till $T \ll T_b$ dominates over the $\coth \left(\frac{\langle \hbar \omega_{\text{TO/LO}} \rangle}{2k_B T} \right)$ term dealing with the equilibrium relaxation dynamics and governing the PL peak red shift. As a result, the *PE* absorption and PL peaks both tend to blue shift with temperature in the broad temperature range of $T = 20 - 100$ K, indicating a strong TO/LO bottleneck effect to occur. However, this general trend is gradually weakened for the PL peak when temperature approaches to that at which the crystalline lattice is getting unfrozen enough to initiate the anharmonic three-phonon TO/LO-phonon decay process involving acoustic phonon branches (Klemens/Ridley process). The resulting deviation of the PL peak temperature dependence from that of the *PE* absorption peak is hence coming from the weakening of TO/LO-phonon bottleneck, which mainly appears for the PL peak since *PE* relaxation (cooling) towards their ground state is required prior to light emission. Alternatively, the *PE* absorption peak temperature dependence mainly reflects the non-equilibrium dynamics, which ignores any relaxation processes. The resulting Stokes shift progresses with increasing temperature, reaching ~ 60 meV at room temperature. the value which presents the energetic difference between the polaronic band gap and *PE* ground-state energy. To verify whether Eq. (12) is relevant to the experimental observations, we re-plotted the temperature dependences of PL-peak position as $E_{PL}^{PE}(T) - E_{PL}^{PE}(20 \text{ K})$, where the lowest

temperature data taken at $T_L = 20$ K is applied instead of that at $T_L = 0$ K (Fig. 5(d)-(f)),

Alternatively, neglecting the spontaneous TO/LO-phonon emission, Eq. (12) describes the PL-peak energy increase with increasing temperature [Fig. 9(a)]. Figure 5(f) confirms the latter tendency by numerically simulated results under $T_b = 450$ K obtained without any fitting parameters. One can clearly see that TO-phonon bottleneck dominates in the orthorhombic phase whereas LO-phonon bottleneck controls the dynamics in the tetragonal/cubic phase. The inflection point is hence a signature of switching between these two regimes.

It is worth noting that the band gap modification energy $E_g^{BGR}(T) - E_g(0)$ varies in the range of $\sim 60 - 100$ meV, which closely matches the polaronic band-edge energy ($\lambda_e + \lambda_h$) ~ 70 meV for LO-phonons, thus suggesting that the blue shift of PL band can be associated with the LO-phonon vibrationally excited polaronic quasiparticles. We note that this mechanism, which is applied to a layer of MAPbBr₃ nanocrystals clearly demonstrating a single PL peak, is completely different to that proposed for thick films demonstrating dual emission features like in bulk single-crystals.^{19,78} Consequently, the proposed mechanism was associated with the thermal expansion of the lattice,⁷⁸ which seems to be irrelevant for nanocrystals where the lattice is flexible enough due to structure phase instability. Furthermore, because λ_e and λ_h for LO-phonons are of the same order as Rashba energies ($E_R \sim 40$ meV),⁷⁹ the polaronic nature of the edge states in MAPbX₃ materials at room temperature should dominate over that associated with the Rashba effect.

To recognize TO/LO-phonon bottleneck on the *pe/ph* and *PE* masses, we consider again the process of TO/LO-phonon emission/reabsorption by hot carriers. LO-phonon emission influences the *pe/ph* masses as $m_{pe,ph}^* = m_{e,h}^* \left[1 + \frac{\langle \alpha_{e,h} \rangle (n+1)}{6} \right]$ ⁷⁴. Accordingly, the whole dynamics can be expressed as

$$\begin{aligned} m_{pe,ph,PE}^* &= m_{e,h,\mu}^* \left[1 + \frac{\langle \alpha_{e,h} \rangle (n+1)}{6} + \frac{\langle \alpha_{e,h} \rangle n_{ne}}{6} \right] = m_{e,h,\mu}^* \\ &\times \left\{ 1 + \frac{\langle \alpha_{e,h,\mu} \rangle}{12} \left[\coth \left(\frac{\langle \hbar \omega_{\text{TO/LO}} \rangle}{2k_B T_L} \right) + \coth \left[\frac{\langle \hbar \omega_{\text{TO/LO}} \rangle}{2k_B (T_b - T_L)} \right] \right] \right\}, \end{aligned} \quad (16)$$

where $m_{\mu}^* = \frac{m_e^* m_h^*}{m_e^* + m_h^*} = 0.077 m_0$ is the reduced exciton mass and $\langle \alpha_{\mu} \rangle = \frac{e^2}{\hbar} \frac{1}{4\pi \varepsilon_0} \sqrt{\frac{m_{\mu}^*}{2 \langle \hbar \omega_{\text{TO/LO}} \rangle}} \left(\frac{1}{\varepsilon_{\infty}} - \frac{1}{\varepsilon_s} \right) = 2.61$ (1.35) is the *PE* coupling coefficient for TO (LO)-phonons. Figures 9(b) and (c) show the numerically simulated results which point out that if TO/LO-phonon bottleneck is neglected ($n_{ne} = 0$), the polaron masses increase with increasing temperature in all the structural phases, that is, the electron (hole, exciton)-phonon coupling is enhanced. TO-phonon bottleneck significantly increases the polaron masses at $T_L = 0$ K followed by their slight decrease with increasing temperature. This behavior indicates that the polaronic quasiparticles are strongly localized in the orthorhombic phase. Alternatively, LO-phonon bottleneck dominating in the tetragonal/cubic phase decreases the polaron masses, making them be almost temperature independent. We note that the *pe/ph* masses in the latter case are only slightly above the electron and hole effective masses, whereas the *PE* mass is less than those.

The effect of TO/LO-phonon bottleneck on the polaron radii can be considered using the polaron radii of Fröhlich polarons at $T_L = 0$ K⁷¹,

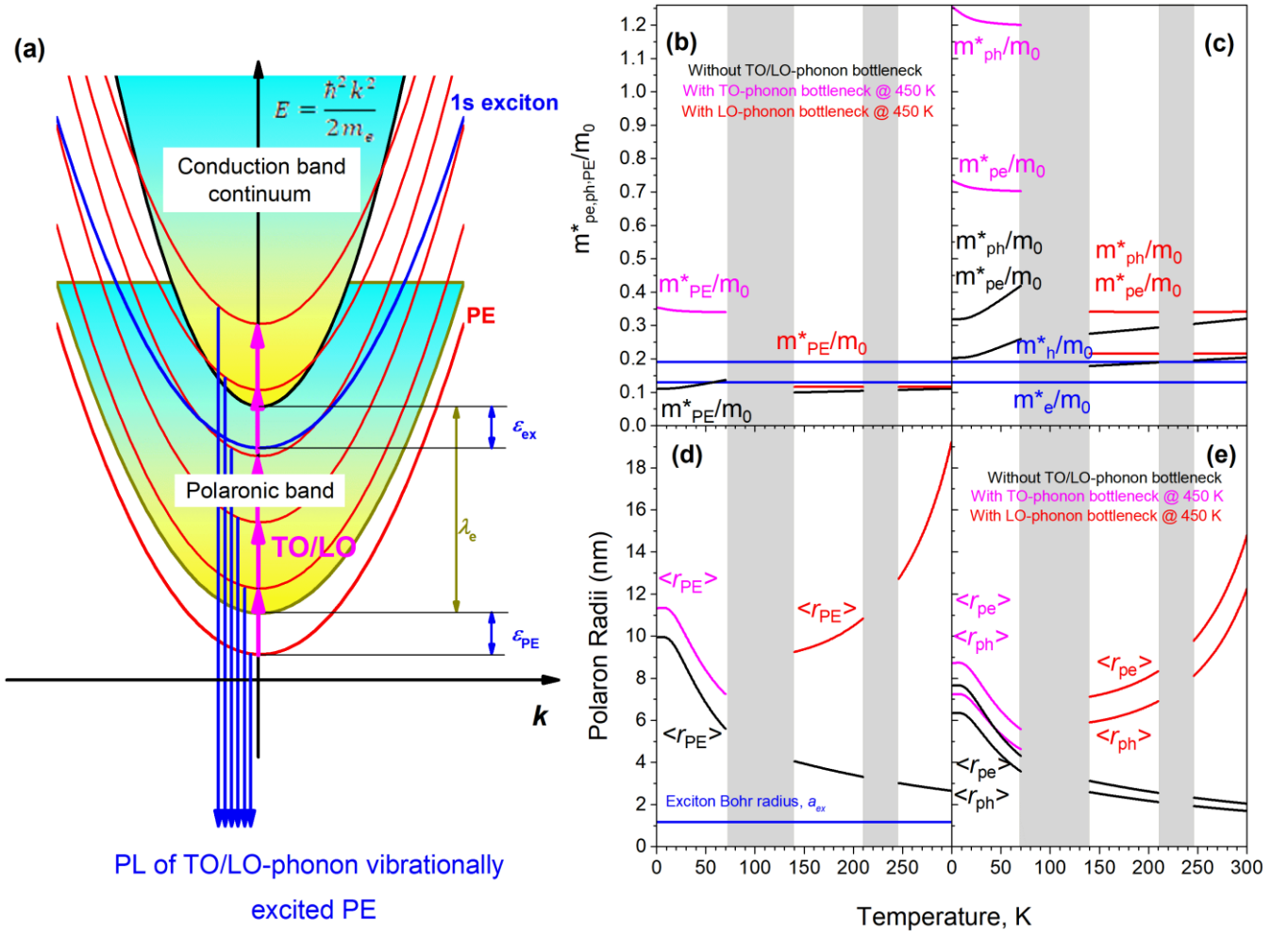


Fig. 9 | PL mechanism and polaron masses and radii. (a) A schematic presentation of CB continuum, 1s exciton, polaronic band, and PE in a layer of 3D MAPbBr₃ nanocrystals. A set of red curves shows a decrease of the initial PE energy ($E_{g.s.}$) upon TO/LO-phonon bottleneck with increasing temperature. (b)-(e) Numerical modeling of the polaron masses [(b) and (c)] and the polaron radii [(d) and (e)] for all the structural phases defined in Fig. 4 without and with TO/LO-phonon bottleneck under $T_b = 450$ K, as indicated by the corresponding colors. The electron and hole effective masses, as well as the exciton Bohr radius are shown in blue.

$$\langle r_{pe,ph,PE}(0) \rangle = \frac{\hbar}{\sqrt{2m_{e,h,\mu}^* \langle \hbar\omega_{TO/LO} \rangle}}. \quad (17)$$

We use the aforementioned parameters to obtain the following equilibrium polaron radii at $T_L = 0$ K when TO-phonons are involved $\langle r_{pe} \rangle = 7.66$ nm, $\langle r_{ph} \rangle = 6.35$ nm, $\langle r_{PE} \rangle = 9.95$ nm and when LO-phonons are involved $\langle r_{pe} \rangle = 3.97$ nm, $\langle r_{ph} \rangle = 3.29$ nm, and $\langle r_{PE} \rangle = 5.16$ nm. These values well match those calculated using the Feynman-Osaka model⁹. The polaron radii are at least

three times greater than the exciton Bohr radius⁸⁰ $a_{ex} = \frac{\hbar^2 \epsilon_0 \epsilon_s}{\mu e^2} = 1.17$ nm, which in turn is about twice the lattice constant (~ 0.59 nm)⁹. These estimates prove the large polaron nature (Fröhlich polaron)⁷¹ of quasiparticles in MAPbBr₃ and imply that the lattice distortions spread over many lattice sites, thus allowing Fröhlich polarons to travel through the lattice as free quasiparticles. We note that the PE radius $\langle r_{PE}(0) \rangle$ only slightly

greater than $\langle r_{pe,ph}(0) \rangle$ because the overlapped polarization clouds of *pe* and *ph* partially cancel each other.⁸¹

The temperature effect on the polaron radii can be treated following the general consideration for polaronic quasiparticles in quantum dots⁸¹ and using the temperature-introducing approach⁷⁴ as

$$\begin{aligned} \langle r_{pe,ph,PE}(T_L) \rangle &= \frac{1}{4\pi\epsilon_0} \frac{e^2}{2\langle \alpha_{e,h,\mu} \rangle (n+1) \langle \hbar\omega_{TO/LO} \rangle} \left(\frac{1}{\epsilon_\infty} - \frac{1}{\epsilon_s} \right) \\ &= \frac{2\langle r_{pe,ph,PE}(0) \rangle}{\coth\left(\frac{\langle \hbar\omega_{TO/LO} \rangle}{2k_B T_L}\right) + 1}. \end{aligned} \quad (18)$$

Subsequently, the TO/LO-phonon bottleneck effect on the polaron radii can be expressed as

$$\langle r_{pe,ph,PE}(T_L) \rangle = \frac{1}{4\pi\epsilon_0} \frac{e^2}{2\langle \alpha_{e,h,\mu} \rangle \langle \hbar\omega_{TO/LO} \rangle}$$

$$\times \left(\frac{1}{\varepsilon_{\infty}} - \frac{1}{\varepsilon_s} \right) \left(\frac{1}{n+1} + \frac{1}{n_{ne}} \right) \\ = 2 \langle r_{pe,ph,PE}(0) \rangle \left\{ \frac{1}{\coth\left(\frac{\langle \hbar \omega_{TO/LO} \rangle}{2k_B T_L}\right) + 1} + \frac{1}{\coth\left[\frac{\langle \hbar \omega_{TO/LO} \rangle}{2k_B (T_b - T_L)}\right] - 1} \right\}. \quad (19)$$

Figures 9(d) and (e) show the corresponding numerical modeling. One can clearly see that without TO/LO-phonon bottleneck [Eq. (18)], the polaron radii shorten with increasing temperature in all the structural phases, thus agreeing with the corresponding increase of the polaron masses.⁷¹ TO-phonon bottleneck slightly increases the polaron radii at $T_L = 0$ K [Eq. (19)], nevertheless, they significantly decrease with increasing temperature in the orthorhombic phase. Once LO-phonon bottleneck begins contributing to the dynamics in the tetragonal/cubic phase, the polaron radii become longer and significantly elongate with increasing temperature. The latter behavior demonstrates the weakening of the electron (hole, exciton)-phonon coupling. The resulting polaron diameters at room temperature exceed the MAPbBr₃ nanocrystal size. This tendency allows the LO-phonon vibrationally excited polaronic quasiparticles to travel through a layer of 3D MAPbBr₃ nanocrystals without scattering on the electrostatic potential fluctuations associated with structural imperfections. Accordingly, the mobility and diffusion of polaronic quasiparticles in a layer MAPbX₃ nanocrystals at room temperature should be significantly enhanced due to LO-phonon bottleneck.

IV. CONCLUSIONS

In this article we highlight several basic approaches which would be interesting to a broad audience of scholars exploring unique PL and transport properties of MAPbX₃ materials. One of them suggests that two-photon-excited PL spectroscopy and electric-field-induced one-photon-excited PL spectroscopy are required to study the structural phase transitions in 3D MAPbX₃ nanocrystals. These techniques are capable of more precisely monitoring the structural phase transitions because the second-order and third-order nonlinear susceptibilities govern the light absorption rates.

Consequently, one can recognize that the structural phase transitions in 3D MAPbBr₃ nanocrystals may occur at about the same temperatures as those in single-crystal MAPbBr₃. However, the orthorhombic-to-tetragonal structural phase transition in 3D MAPbBr₃ nanocrystals, unlike in single-crystal MAPbX₃, is spread out over the broad temperature range of $T \sim 70 - 140$ K due to the structural phase instability induced by local field fluctuations when free rotations of MA ions are no longer restricted strongly by long-range polar order. The resulting configurational entropy loss and the liquid-like motion of MA cations in 3D MAPbBr₃ nanocrystals can be even enhanced by the interfacial electric field arising due to charge separation at the MAPbBr₃/ZnO heterointerface, extending the range of the orthorhombic-to-tetragonal structural phase instability from $T \sim 70$ to 230 K and significantly shifting the tetragonal-to-cubic phase transition towards higher temperatures exceeding room temperature.

The latter effect is found to be dependent on the ZnO layer thickness and the photoexcited carrier density, thus allowing one to control the structural phase instability range in 3D MAPbBr₃ nanocrystals. Finally, we conclude that a stepwise shift of the PL band with temperature observed for single-crystal MAPbX₃ is no longer an indication of the structural phase transition in 3D

MAPbBr₃ nanocrystals because of negligible distortions of PbX₆ octahedra under the structural phase instability regime. On the contrary, the nearly monotonic blue shift of PL band with increasing temperature in a fully encapsulated single layer of 20-nm-sized 3D MAPbBr₃ nanocrystals seems to result rather from the heating effect under TO/LO phonon bottleneck than that being induced by the progressive PbX₆ octahedra distortions.

Furthermore, we point out that two-photon-excited PL spectroscopy and electric-field-induced one-photon-excited PL spectroscopy mainly characterize PL excitation in the nanocrystal core, contrary to conventional one-photon-excited PL spectroscopy dealing with PL excitation in both the nanocrystal core and the nanocrystal surface. Consequently, because the ratio of the surface-to-core PL contributions for nanocrystals is large enough and because the surface states are less sensitive to the structural phase transitions in the core, the structural phase transitions in MAPbX₃ nanocrystals can be significantly masked by PL from the surface states when conventional one-photon excitation is applied. This circumstance together with the structural phase instability occurring within the broad temperature range seems to be a reason why the structural phase transitions in MAPbX₃ nanocrystals have never been observed.

We also confirmed that the photoexcited carriers responsible for the light-emitting and transport properties of a layer of 3D MAPbBr₃ nanocrystals are the polaronic quasiparticles, which can be TO/LO-phonon vibrationally excited to the higher-energy states owing to TO/LO-phonon bottleneck. Consequently, PL from MAPbBr₃ nanocrystals results from the recombination of *PEs*, which can emit light either in the ground or TO/LO-phonon vibrationally excited states, thus giving rise to the ~ 100 meV blue-shift of PL-peak usually appearing in MAPbBr₃ nanocrystals with increasing temperature. We note that this polaronic nature of the edge states in MAPbX₃ nanocrystals becomes dominant exclusively at higher temperatures (including room temperature) just because energies of the TO/LO-phonon vibrationally excited polaronic quasiparticles (~ 100 meV) significantly exceeds the ground-state polaron ($\lambda_e, \lambda_h \leq \sim 40$ meV) and Rashba energies ($E_R \sim 40$ meV). Alternatively, the Rashba spin-split nature of the edge states in MAPbX₃ nanocrystals is expected to be dominant only at low temperature when the Rashba energy might exceed energies of the TO/LO-phonon vibrationally excited polaronic quasiparticles.

Additionally, we showed that at room temperature owing to LO-phonon bottleneck, the polaron masses diminish and polaron radii increase. This behavior creates unique conditions for the TO/LO-phonon vibrationally excited polaronic quasiparticles to travel long distances without scattering on electrostatic potential fluctuations governed by structural imperfections.

ACKNOWLEDGEMENTS

This work was supported by the National Key Research and Development Program of China administrated by the Ministry of Science and Technology of China (No. 2016YFB0401702), the Guangdong High-Level Science and Technology Discipline Development Project, Guangdong University Key Laboratory for Advanced Quantum Dot Displays and Lighting (No. 2017KSYS007), the National Natural Science Foundation of China with Grant Nos.11574130 and 61674074, Development and Reform Commission of Shenzhen Project (No. [2017]1395), Shenzhen Peacock Team Project (No. KQTD2016030111203005), Shenzhen Key Laboratory of

Advanced quantum dot Displays and Lighting (No. ZDSYS201707281632549), Shenzhen Innovation Project (No. JCYJ20160301113356947, JCYJ20150930160634263, JCYJ20160301113356947). R. Chen acknowledges the support from national 1000 plan for young talents.

REFERENCES

- H. Zhu, K. Miyata, Y. Fu, J. Wang, P. P. Joshi, D. Niesner, K. W. Williams, S. Jin, and X.-Y. Zhu, *Sci.* **353**, 1409 (2016).
- Y. Yang, D. P. Ostrowski, R. M. France, K. Zhu, J. van de Lagemaat, J. M. Luther, and M. C. Beard, *Nat. Photonics* **10**, 53 (2016).
- J. Fu, Q. Xu, G. Han, B. Wu, C. H. A. Huan, M. L. Leek, and T. C. Sum, *Nat. Commun.* **8**, 1300 (2017).
- J. Yang, X. Wen, H. Xia, R. Sheng, Q. Ma, J. Kim, P. Tapping, T. Harada, T. W. Kee, F. Huang, Y.-B. Cheng, M. Green, A. Ho-Baillie, S. Huang, S. Shrestha, R. Patterson, and G. Conibeer, *Nat. Commun.* **8**, 14120 (2017).
- S. D. Stranks, G. E. Eperon, G. Grancini, C. Menelaou, M. J. P. Alcocer, T. Leijtens, L. M. Herz, A. Petrozza, and H. J. Snaith, *Sci.* **342**, 341 (2013).
- H. Oga, A. Saeki, Y. Ogomi, S. Hayase, and S. Seki, *J. Am. Chem. Soc.* **136**, 13818 (2014).
- X. Y. Zhu, and V. Podzorov, *J. Phys. Chem. Lett.* **6**, 4758 (2015).
- J. Even, L. Pedesseau, C. Katan, M. Kepenekian, J.-S. Laurent, D. Sapori, and E. Deleporte, *J. Phys. Chem. C* **119**, 10161 (2015).
- K. Miyata, D. Meggiolaro, M. T. Trinh, P. P. Joshi, E. Mosconi, S. C. Jones, F. De Angelis, and X.-Y. Zhu, *Sci. Adv.* **3**, e1701217 (2017).
- A. J. Neukirch, W. Nie, J.-C. Blancon, K. Appavoo, H. Tsai, M. Y. Sfeir, C. Katan, L. Pedesseau, J. Even, J. J. Crochet, G. Gupta, A. D. Mohite, and S. Tretiak, *Nano Lett.* **16**, 3809 (2016).
- M. Park, A. J. Neukirch, S. E. Reyes-Lillo, M. Lai, S. R. Ellis, D. Dietze, J. B. Neaton, P. Yang, S. Tretiak, and R. A. Mathies, *Nat. Commun.* **9**, 2525 (2018).
- B. Li, Y. Kawakita, Y. Liu, M. Wang, M. Matsuura, K. Shibata, S. Ohira-Kawamura, T. Yamada, S. Lin, K. Nakajima, S. Liu, *Nat. Commun.* **8**, 16086 (2017).
- C. Chen, X. Hu, W. Lu, S. Chang, L. Shi, L. Li, H. Zhong, and J.-B. Han, *J. Phys. D: Appl. Phys.* **51**, 045105 (2018).
- K.-H. Wang, L.-C. Li, M. Shellaiah, and K. W. Sun, *Sci. Rep.* **7**, 13643 (2017).
- H. Linnenbank, M. Saliba, L. Gui, B. Metzger, S. G. Tikhodeev, J. Kadro, G. Nasti, A. Abate, A. Hagfeldt, M. Graetzel, and H. Giessen, *Opt. Mater. Express.* **8**, 511 (2018).
- N. Sestu, M. Cadelano, V. Sarritzu, F. Chen, D. Marongiu, R. Piras, M. Mainas, F. Quochi, M. Saba, A. Mura, and G. Bongiovanni, *J. Phys. Chem. Lett.* **6**, 4566 (2015).
- H. Kunugita, T. Hashimoto, Y. Kiyota, Y. Udagawa, Y. Takeoka, Y. Nakamura, J. Sano, T. Matsushita, T. Kondo, T. Miyasaka, and K. Ema, *Chem. Lett.* **44**, 852 (2015).
- B. Yang, W. Ming, M.-H. Du, J. K. Keum, A. A. Puzos, C. M. Rouleau, J. Huang, D. B. Geohegan, X. Wang, and K. Xiao, *Adv. Mater.* **30**, 1705801 (2018).
- F. Zhao, X. Gao, X. Fang, Y. D. Glinka, X. Feng, Z. He, Z. Wei, and R. Chen, *Adv. Mater. Interfaces* **5**, 1800301 (2018).
- I. Anusca, S. Balciunas, P. Gemeiner, S. Svirskas, M. Sanlialp, G. Lackner, C. Fettkenhauer, J. Belovickis, V. Samulionis, M. Ivanov, B. Dkhil, J. Banys, V. V. Shvartsman, and D. C. Lupascu, *Adv. Energy Mater.* **7**, 1700600 (2017).
- B. T. Diroll, P. Guo, and R. D. Schaller, *Nano Lett.* **18**, 846 (2018).
- A. E. Osherov, M. Hutter, K. Galkowski, R. Brenes, D. K. Maude, R. J. Nicholas, P. Plochocka, V. Bulovic, T. J. Savenije, and S. D. Stranks, *Adv. Mater.* **28**, 10757 (2016).
- A. M. Soufiani, F. Huang, P. Reece, R. Sheng, A. Ho-Baillie, and M. A. Green, *Appl. Phys. Lett.* **107**, 231902 (2015).
- D. Li, G. Wang, H.-C. Cheng, C.-Y. Chen, H. Wu, Y. Liu, Y. Huang, and X. Duan, *Nat. Commun.* **7**, 11330 (2016).
- A. Dobrovolsky, A. Merdasa, E. L. Unger, A. Yartsev, and I. G. Scheblykin, *Nat. Commun.* **8**, 34 (2017).
- W.-L. Ong, S. M. Rupich, D. V. Talapin, A. J. H. McGaughey, and J. A. Malen, *Nat. Mater.* **12**, 410 (2013).
- O. Yaffe, Y. Guo, L. Z. Tan, D. A. Egger, T. Hull, C. C. Stoumpos, F. Zheng, T. F. Heinz, L. Kronik, M. G. Kanatzidis, J. S. Owen, A. M. Rappe, M. A. Pimenta, and L. E. Brus, *Phys. Rev. Lett.* **118**, 136001 (2017).
- J. M. Frost, K. T. Butler, and A. Walsh, *APL Mater.* **2**, 081506 (2014).
- I. Levchuk, P. Herre, M. Brandl, A. Osvet, R. Hock, W. Peukert, P. Schweizer, E. Spiecker, M. Batentschuka, and C. J. Brabec, *Chem. Commun.* **53**, 244 (2017).
- G. Walters, B. R. Sutherland, S. Hoogland, D. Shi, R. Comin, D. P. Sellan, O. M. Bakr, and E. H. Sargent, *ACS Nano* **9**, 9340 (2015).
- Y. D. Glinka, S. Babakiray, T. A. Johnson, A. D. Bristow, M. B. Holcomb, and D. Lederman, *Appl. Phys. Lett.* **103**, 151903 (2013).
- Y. D. Glinka, Z. Sun, M. Eremenchouk, M. N. Leuenberger, A. D. Bristow, S. T. Cundiff, A. S. Bracker, and X. Li, *Phys. Rev. B* **88**, 075316 (2013).
- M. V. Kovalenko, L. Protesescu, and M. I. Bodnarchuk, *Sci.* **358**, 745 (2017).
- F. Yan, J. Xing, G. Xing, L. Quan, S. T. Tan, J. Zhao, R. Su, L. Zhang, S. Chen, Y. Zhao, A. Huan, E. H. Sargent, Q. Xiong, and H. V. Demir, *Nano Lett.* **18**, 3157 (2018).
- N. Cho, F. Li, B. Tureli, L. Sinatra, S. P. Sarmah, M. R. Parida, M. I. Saidaminov, B. Murali, V. M. Burlakov, A. Goriely, O. F. Mohammed, T. Wu, and O. M. Bakr, *Nat. Commun.* **7**, 13407 (2016).
- Q. Zhu, K. Zheng, M. Abdellah, A. Generalov, D. Haase, S. Carlson, Y. Niu, J. Heimdahl, A. Engdahl, M. E. Messing, T. Pullerits, and S. E. Canton, *Phys. Chem. Chem. Phys.* **18**, 14933 (2016).
- V. Malgras, J. Henzie, T. Takeia, and Y. Yamauchi, *Chem. Commun.* **53**, 2359 (2017).
- S. Gonzalez-Carrero, R. E. Galian, and J. Perez-Prieto, *Opt. Express.* **24**, A285 (2016).
- B. Xu, W. Wang, X. Zhang, W. Cao, D. Wu, S. Liu, H. Dai, S. Chen, K. Wang, and X. W. Sun, *J. Mater. Chem. C* **5**, 6123 (2017).
- A. M. A. Leguy, P. Azarhoosh, M. I. Alonso, M. Campoy-Quiles, O. J. Weber, J. Yao, D. Bryant, M. T. Weller, J. Nelson, A. Walsh, M. van Schilfgaarde, and P. R. F. Barnes, *Nanoscale* **8**, 6317 (2016).
- M. Kato, T. Fujiseki, T. Miyadera, T. Sugita, S. Fujimoto, M. Tamakoshi, M. Chikamatsu, and H. Fujiwara, *J. Appl. Phys.* **121**, 115501 (2017).
- D. Pal, A. Mathur, A. Singh, J. Singhal, A. Sengupta, S. Dutta, S. Zollner, and S. Chattopadhyay, *J. Vac. Sci. & Tech. A* **35**, 01B108 (2017).
- P. K. Ghorai, and D. V. Matyushov, *J. Chem. Phys.* **124**, 144510 (2006).
- S. Neutzner, F. Thouin, D. Cortecchia, A. Petrozza, C. Silva, and A. R. S. Kandada, *Phys. Rev. Mater.* **2**, 064605 (2018).
- K. Tanaka, T. Takahashi, T. Ban, T. Kondo, K. Uchida, and N. Miura, *Solid State Commun.* **127**, 619 (2003).
- A. M. A. Leguy, A. R. Goni, J. M. Frost, J. Skelton, F. Brivio, X. Rodriguez-Martinez, O. J. Weber, A. Pallipurath, M. I. Alonso, M. Campoy-Quiles, M. T. Weller, J. Nelson, A. Walsh, and P. R. F. Barnes, *Phys. Chem. Chem. Phys.* **18**, 27051 (2016).
- T. Glaser, C. Muller, M. Sendner, C. Krekeler, O. E. Semonin, T. D. Hull, O. Yaffe, J. S. Owen, W. Kowalsky, A. Pucci, and R. Lovrincic, *J. Phys. Chem. Lett.* **6**, 2913 (2015).
- C. M. Iaru, J. J. Geuchies, P. M. Koenraad, D. Vanmaekelbergh, and A. Y. Silov, *ACS Nano* **11**, 11024 (2017).
- M. Ledinsky, P. Löper, B. Niesen, J. Holovsky, S.-J. Moon, J.-H. Yum, S. D. Wolf, A. Fejfar, and C. Ballif, *J. Phys. Chem. Lett.* **6**, 401 (2015).
- D. Curie, *Luminescence in Crystals* (Wiley, New York, 1963).
- P. S. Whitfield, N. Herron, W. E. Guise, K. Page, Y. Q. Cheng, I. Milas, and M. K. Crawford, *Sci. Rep.* **6**, 35685 (2016).
- K.-Y. Kou, Y.-E. Huang, C.-H. Chen, and S.-W. Feng, *Beilstein J. Nanotechnol.* **7**, 75 (2016).
- C. Kittel, *Introduction to Solid State Physics, 7th ed.*, (John Wiley & Sons, New York, 1996).

- ⁵⁴H.-W. Chen, D. P. Gulo, Y.-C. Chao and H.-L. Liu, *Sci. Rep.* **9**, 18253 (2019).
- ⁵⁵R. W. Boyd, *Nonlinear Optics, 3th ed.*, (Academic Press, Orlando, 2008).
- ⁵⁶Y. D. Glinka, N. H. Tolk, X. Liu, Y. Sasaki, and J. K. Furdyna, *Appl. Phys. Lett.* **91**, 231104 (2007).
- ⁵⁷Y. D. Glinka, N. H. Tolk, X. Liu, Y. Sasaki, and J. K. Furdyna, *J. Appl. Phys.* **103**, 043708 (2008).
- ⁵⁸Y. D. Glinka, S. Babakiray, T. A. Johnson, M. B. Holcomb, and D. Lederman, *Nat. Commun.* **7**, 13054 (2016).
- ⁵⁹Y. Kawamura, H. Mashiyama, and K. Hasebe, *J. Phys. Soc. Jpn.* **71**, 1694 (2002).
- ⁶⁰M. T. Weller, O. J. Weber, P. F. Henry, A. M. Di Pumpo, T. C. Hansen, *Chem. Commun.* **51**, 4180 (2015).
- ⁶¹P. Y. Yu, and M. Cardona, *Fundamentals of Semiconductors* (Springer, Heidelberg, 2010).
- ⁶²Y. D. Glinka, V. Y. Degoda, S. N. Naumenko, *J. Non-Crystal. Sol.* **152**, 219 (1993).
- ⁶³R. P. Chin, Y. R. Shen, V. Petrova-Koch, *Sci.* **270**, 776 (1995).
- ⁶⁴Y. D. Glinka, K-W. Lin, and S. H. Lin, *Appl. Phys. Lett.* **74**, 236 (1999).
- ⁶⁵Y. D. Glinka, K-W. Lin, H-C. Chang and S. H. Lin, *J. Phys. Chem.* **103**, 4251 (1999).
- ⁶⁶A. D. Wright, C. Verdi, R. L. Milot, G. E. Eperon, M. A. Perez-Osorio, H. J. Snaith, F. Giustino, M. B. Johnston, and L. M. Herz, *Nat. Commun.* **7**, 11755 (2016).
- ⁶⁷F. Cadiz, E. Courtade, C. Robert, G. Wang, Y. Shen, H. Cai, T. Taniguchi, K. Watanabe, H. Carrere, and D. Lagarde, *Phys. Rev. X* **7**, 021026 (2017).
- ⁶⁸Y. P. Varshni, *Physica* **34**, 149 (1967).
- ⁶⁹L. Vina, S. Logothetidis, and M. Cardona, *Phys. Rev. B* **30**, 1979 (1984).
- ⁷⁰J. Casas-Vazquez, D. Jou, *Rep. Prog. Phys.* **66**, 1937 (2003).
- ⁷¹J. T. Devreese, and A. S. Alexandrov, *Rep. Prog. Phys.* **72**, 066501 (2009).
- ⁷²T. Ivanovska, C. Dionigi, E. Mosconi, F. De Angelis, F. Liscio, V. Morandi, and G. Ruani, *J. Phys. Chem. Lett.* **8**, 3081 (2017).
- ⁷³E. Burovski, H. Fehske, and A. S. Mishchenko, *Phys. Rev. Lett.* **101**, 116403 (2008).
- ⁷⁴T. Fulton, *Phys. Rev.* **103**, 1712 (1956).
- ⁷⁵S. Netzner, F. Thouin, D. Cortecchia, A. Petrozza, C. Silva, and A. R. S. Kandada, *Phys. Rev. Mater.* **2**, 064605 (2018).
- ⁷⁶K. O'onnell, and X. Chen, *Appl. Phys. Lett.* **58**, 2924 (1991).
- ⁷⁷A. M. Soufiani, F. Huang, P. Reece, R. Sheng, A. Ho-Baillie, and M. A. Green, *Appl. Phys. Lett.* **107**, 231902 (2015).
- ⁷⁸M. I. Dar, G. Jacopin, S. Meloni, A. Mattoni, N Arora, A. Boziki, S M. Zakeeruddin, U. Rothlisberger, M. Grätzel, *Sci. Adv.* **2**, 1601156 (2016).
- ⁷⁹Y. Zhai, S. Baniya, C. Zhang, J. Li, P. Haney, C.-X. Sheng, E. Ehrenfreund, and Z. V. Vardeny, *Sci. Adv.* **3**, 1700704 (2017).
- ⁸⁰R. Knox, *Theory of excitons, Solid State Physics: Supplement 5* (Academic Press, 1963).
- ⁸¹R. T. Senger, and K. K. Bajaj, *Phys. Rev. B* **68**, 045313 (2003).

Author contributions

Y.D.G.: proposed the method of fully encapsulating MAPbBr₃ nanocrystals between the two sapphire plates. R.Cai: prepared all the samples, participated in the SEM, TEM, XRD characterization, and in paper writing. Y.D.G. and X.G.: designed the optical experiments and created the optical setup. X.G. and D.W.: performed all the optical experiments. D.W.: performed the SEM, TEM, and XRD characterization experiments, initially treated the optical experiment data, and participated in paper writing. The optical measurements were performed in the laboratory hosted by R.Chen. Y.D.G: mentored students and postdocs, analyzed the data, performed theoretical treatment and numerical simulations and wrote the paper. X.W.S.: guided the research and supervised the project. All authors contributed to discussions.

Additional information

Supplementary Information accompanies this paper at <http://www.nature.com>

Competing financial interests: The authors declare no competing financial interests.